



ACADÉMIE  
DES SCIENCES  
INSTITUT DE FRANCE

# *Comptes Rendus*

---

## *Physique*


Marc Gabay

**Topological phases driven by orbital entanglement in Transition Metal Oxide Perovskite interfaces**

Volume 25 (2024), p. 303-327

Online since: 19 September 2024

<https://doi.org/10.5802/crphys.190>

 This article is licensed under the  
CREATIVE COMMONS ATTRIBUTION 4.0 INTERNATIONAL LICENSE.  
<http://creativecommons.org/licenses/by/4.0/>



*The Comptes Rendus. Physique are a member of the  
Mersenne Center for open scientific publishing*  
[www.centre-mersenne.org](http://www.centre-mersenne.org) — e-ISSN : 1878-1535



Research article / *Article de recherche*

# Topological phases driven by orbital entanglement in Transition Metal Oxide Perovskite interfaces

*Phases topologiques induites par intrication des composantes orbitales aux interfaces d'oxydes de métaux de transition*

Marc Gabay<sup>a</sup>

<sup>a</sup> Laboratoire de Physique des Solides, Université Paris Saclay, CNRS UMR 8502,  
F-91405 Orsay Cedex, France  
E-mail: marc.gabay@universite-paris-saclay.fr

**Abstract.** The deceptively simple crystallographic structure of early transition metal oxide perovskites belies the complexity and variety of electronic, magnetic and structural phases that they display. Structural defects, rotations, tilts, deformations of the oxygen-transition metal element octahedra help explain many of these phenomena. Another key player is the orbital degree of freedom of the d-ion. It may lead to a quantum entanglement of the materials electronic wavefunctions which promotes topological states in low dimensional geometries. In this report we present a study of select topological properties at surfaces or heterostructure interfaces of a subset of these perovskites when the orientation of the structure is along the (001) or (111) direction. In contrast to the extensively studied classes of topological insulators, topology in these systems is a characteristic property of the conducting regime, thus endowing the compounds with potential spintronic and quantum computing functionalities. We conclude this communication with a personal tribute to Gérard Toulouse (in French).

**Résumé.** En dépit de l'apparente simplicité de leur structure cristallographique, les perovskites de métaux de transition présentent une grande richesse et complexité de phases électroniques, magnétiques et structurales. L'existence de différents types de défauts, de rotations et déformations des octaèdres oxygène-ion de transition expliquent en partie ce phénomène. De plus, le caractère d des fonctions d'ondes de l'ion de transition introduit un degré de liberté supplémentaire, susceptible de mener à l'intrication des fonctions d'onde du composé. Ceci confère à ces matériaux des propriétés topologiques en dimension réduite. Nous présentons ici quelques unes des caractéristiques topologiques aux interfaces et surfaces d'hétérostructures de certaines perovskites, lorsque la croissance est effectuée selon les orientations (001) et (111). Contrairement au cas très étudié des isolants topologiques, la topologie se manifeste dans le régime métallique, avec pour conséquence un réel potentiel sur le plan de l'ingénierie spintronique et du calcul quantique. Nous concluons par un hommage personnel à la mémoire de Gérard Toulouse.

**Keywords.** Materials Science, Theory, Perovskites, Interfaces, Topology, Spintronic.

**Mots-clés.** Science des matériaux, Théorie, Perovskites, Interfaces, Topologie, Spintronique.

*Manuscript received 15 March 2024, revised 22 May 2024, accepted 27 May 2024.*

## 1. Introduction

More than 50 years ago, in his Nobel address, Herbert Kroemer stated that “the interface is the device”. He was referring to the thin conducting channel confined near the interface of a semiconducting heterostructure. In 2004, a bold experiment performed at Bell Labs [1] opened the door to a potentially similar technological breakthrough, this time in a perovskite transition metal oxide heterostructure. The chemical composition of a prototypic perovskite material is of the form  $ABO_3$ , where A is an alkaline or earth-alkaline element (e.g. K, Ba, Sr,..) and B is a early transition metal ion (e.g. Ti, Cr, V, Ta, ...). In the undistorted structure, the d-ions sit at the center of an octahedral cage of O ions. d-electron hops between neighboring d-sites involve an excursion onto the intermediate O site. Valence (conduction) bands have a predominantly O (d-type) character and the site energy difference between the the two types of elements is typically on the order of 3-4 eV. For these reasons, bulk  $SrTiO_3$  (STO) is a large gap band insulator. Remarkably, Ohtomo and Hwang’s 2004 experiment demonstrated that upon growing a thin film of  $LaAlO_3$  (LAO) on top of STO, both being robust paramagnetic insulators, one observed the appearance of a metallic sheet close to the interface. In the following years, superconductivity [2] was evidenced, claims of ferromagnetism within the metallic channel were made [3–8] and, most importantly, a large spin-orbit energy was detected in this interfacial two-dimensional electron sheet (2DES) [9, 10]. All of these features can be broadly tuned with a gate voltage [11]. The LAO overlayer plays the role of a gate dielectric and the few nanometer thin 2DES allows for an electric field to penetrate the conducting layer. The heterostructure is essentially a spintronic transistor [12–14]. Appealing features of the 2DES are a carrier concentration 2-3 orders of magnitude larger than for conventional field effect transistors, little leakage current which is desirable for low power technologies [15, 16]. The value of the room temperature mobility still needs to be increased in order to bring it closer to that of GaAs semiconductors. Significant advances in materials science made it possible to grow heterostructures layer by layer in a controlled, almost defect-free fashion [17, 18]. Further emergent phenomena at the interface, such as ferroelectricity, colossal magnetoresistance, multiferroelectricity, ferromagnetic polarization, can be imparted to the 2DES by selecting an appropriate type of perovskite (e.g  $BaTiO_3$ ,  $KTaO_3$ ) [19] and capping layer (e.g Al, Gd,  $GdTiO_3$ ,  $\gamma$ -aluminate, EuO,  $LaTiO_3$ ,  $SmTiO_3$ ) [20–22]. From an engineering perspective these heterostructures have been appropriately branded functional oxides [23].

The mechanism underlying the formation of the 2DES is still being debated [24–28]. Two main scenarios have been proposed and, based on the experimental data, it is plausible that both of these are at play: electronic reconstruction (also referred to as polar catastrophe) and O vacancy. In either case, there is an electron density build-up on the  $ABO_3$  side of the interface when the capping film exceeds a critical thickness (four unit cells of LAO for the LAO-STO heterostructure). Theoretical investigations of these systems are essentially based on either density functional calculations [29–31] or tight-binding modeling which include Coulomb interactions [32], often complemented by Poisson-Schrodinger algorithm [33]. In order to assign numerical values to the relevant parameters, the electronic band structure derived from the latter approach is compared to spectra obtained by Angle Resolved Photoemission Spectroscopy (ARPES)[34–37]. Relevant terms that need to be included in model hamiltonians are the crystal field splitting of the d orbitals, the confinement energy which arises from the quantum well-type electronic motion in the direction perpendicular to the interface, the kinetic energy of carriers within the 2DES, Coulomb interactions between electrons, the atomic spin-orbit energy (SOC) [38] of the d ions and, last but not least, a crucial contribution named “orbital mixing” (OM) [39–42] which stems from the breaking of inversion symmetry at the interface. The electric potential difference across the interface and the steric constraint due to the difference in chemical formula cause a rumpling of the boundary layers. Consequently, the B-O-B bond angle deviates from  $180^\circ$  such

that electron hops from one B site onto a neighboring one may involve two different d orbitals. For the undistorted structure this would be forbidden by symmetry. The concomitant presence of the OM and SOC interactions produces a surface spin-orbit contribution which is called the Rashba spin orbit interaction [43]. The simplest linear form is  $\alpha(\mathbf{k} \times \boldsymbol{\sigma})$  where  $\mathbf{k}$  is the d electron momentum parallel to the interface,  $\boldsymbol{\sigma}$  its spin and  $\alpha$  is the Rashba coefficient which depends on the electric field and bond angle at the interface. The Rashba contribution entangles the spin and the charge in the 2DES, which opens the perspective of spintronic transport within the conducting sheet according to the so called Edelstein effect [44, 45]

In the absence of defects (charge or spin), the band structure of the 2DES is characterized by Bloch states. Yet, as the eigenvectors in k space have several components because of spin and/or of a multi-orbital band structure, the phase of the wavefunctions may become singular within the Brillouin zone (BZ). This is a quantum geometric effect which gives rise to a (quantum) metric contribution and possibly also to a Berry phase. It is akin to the magnetic-like flux picked up by the electronic wavefunction in momentum space, in the presence of real space defects. While Hall effects were manifestations of topology in solid state matter subjected to a magnetic field, time reversal symmetric topological quantum matter in the context of Bloch bands emerged in the early years 2000, first in the form of topological insulators and topological superconductors (there is a similarity between their hamiltonians) [46–50] then of topological semimetals (Dirac, Weyl) [51, 52]. The emergence of topology in quantum materials is linked to the symmetries of the hamiltonian. The most common are time reversal, inversion, parity. Early examples of topological insulators involve a band inversion process. Chemical substitution or spin orbit tuning produce a band inversion between the top of the valence band and the bottom of the conduction band and a symmetry breaking term opens up a gap. The parity of the states is usually even for the bonding (valence) levels and odd for the antibonding (conduction) levels. Hence, there is a region in k space in both the valence and conduction bands where the parity is opposite to that of the rest of the band and the gap protects the states in that region against mixing with the other states. If the chemical potential falls within the gap, the material is insulating, but its edges are “metallic”, due to the appearance of edge states. When no bias voltage is applied to the material, the total electric current at the edge is zero but a chiral spin current propagates (spin Hall effect). This is the signature of a stable topological state characterized by a discrete index  $Z_2 = x + 1$  [53–55] (A system which is invariant under time reversal and k space inversion operations does not sustain a Berry curvature). A Weyl semimetal is an extension of the topological insulator such that, in the topological regime, the gap closes at two- or two pairs- of points depending on whether either time reversal or inversion symmetries or both, are broken. These nodes are sources of Berry monopoles. On the surface of the Weyl semimetal, there exists a Fermi arc ending at two- (or two pairs-) of points – the projections of the nodes onto the surface. The Dirac semimetal is the limit of the Weyl semimetal when the nodes (or pairs of nodes) coalesce into a single (or double) Dirac point.

In the above examples, the states that are considered belong to valence and conduction bands. In this report, we underscore the role of topology in situations when only the conduction bands are involved, i.e. in the metallic regime of the 2DES. In Section 2 we discuss the occurrence of Dirac points within the conduction band of (001) oriented STO and LAO/STO. We further highlight the presence of topological textures (spin, orbital) in these same systems and indicate that they lead to spintronic manifestations [56]. Section 3 discusses select topological properties of the (111) oriented structures and present several new results pertaining to that orientation. Much effort has also been devoted to extending these analyses to the case of interacting systems [57]. Strong interactions tend to localize charge carriers in real space. The theoretical framework that we discussed so far is developed in k space. Working out the balance between these seemingly competing effects is not a trivial problem and we will not consider this situation in our report.

We conclude the paper with a personal tribute to Gérard Toulouse. The central role of topology that he advocated for condensed matter systems in real space has a counterpart in momentum space.

## 2. Topology in the (001) orientation

In this section, we show that the 2DES located on the STO side of the interface with a thin film of LAO or Al, Gd, . . . hosts topological states. As we discussed in the introduction, we first construct a tight binding hamiltonian the parameters of which yield a spectrum quantitatively matching the ARPES bands [41, 42, 58]. Owing to the local octahedral symmetry of the Ti ions and to the directional character of the Ti - O bonds, d orbitals are split into an  $e_g$  doublet and a  $t_{2g}$  triplet separated by a 2.5 eV gap. Relevant states of the 2DES involve the  $t_{2g}$  states  $d_{xy}$ ,  $d_{yz}$ ,  $d_{xz}$ . Quantization of the motion perpendicular to the interface implies that the energies at  $\Gamma$  (the center of the BZ) form a discrete sequence of levels. Based on ARPES data, the first two levels have a  $d_{xy}$  character, the next ones a  $d_{yz}$  or  $d_{xz}$  character [34, 59, 60]. Symmetry requires that hops from one Ti site onto a neighboring one preserve the orbital character of the electron wavefunction. These hops involve an intermediate excursion onto an O site; for a  $d_{xy}$  orbital, the Ti-O overlaps in the  $x$  and  $y$  directions give a hopping amplitude  $t \sim 0.388$  eV. For the  $d_{yz}$  or  $d_{xz}$  orbitals hops along the  $y$  ( $x$ ) direction involve an amplitude  $t$  but along  $x$  ( $y$ ) the overlap with the O site gives zero. However, due to residual direct Ti-Ti hopping, there is still a small  $t_h \sim 0.031$  eV contribution.

$$\begin{cases} \epsilon_{d_{xy1}} = 2t(2 - \cos k_x - \cos k_y) + \epsilon_1 \\ \epsilon_{d_{xy2}} = 2t(2 - \cos k_x - \cos k_y) + \epsilon_{p1} \\ \epsilon_{d_{yz}} = 2t(1 - \cos k_y) + 2t_h(1 - \cos k_x) + \epsilon_2 \\ \epsilon_{d_{xz}} = 2t(1 - \cos k_x) + 2t_h(1 - \cos k_y) + \epsilon_2 \end{cases} \quad (1)$$

where the in-plane wave-vector components  $k_x$  and  $k_y$  are dimensionless (momenta times  $a$ , the lattice parameter). For the STO/Al interface,  $\epsilon_1 \sim -0.205$  eV,  $\epsilon_{p1} \sim -0.105$  eV,  $\epsilon_2 \sim -0.0544$  eV are the values of the energies of the quantized levels at  $\Gamma$ . For bulk states, the three  $t_{2g}$  energies would be equal at  $\Gamma$ . Figure 1 shows that along the [100] direction of the BZ, the  $d_{yz}$  band intersects both  $d_{xy}$  bands. Along the [110] direction  $d_{yz}$  and  $d_{xz}$  branches are degenerate so that all three  $d_{xy}$ ,  $d_{yz}$ ,  $d_{xz}$  bands intersect at finite values of the momenta. In the vicinity of this crossing point, the dispersion is linear in  $k$ , such that we have a ‘‘triple’’ Dirac point. This special point plays the role of an effective  $\Gamma$  point and we label it  $\Gamma_{DP}$ . Due to the  $C_4$  rotational symmetry, there are four such  $\Gamma_{DP}$  points in the BZ, two along the [110] direction and two along the  $[\bar{1}10]$  direction. As seen in Figure 1 the lowest energy crossing involves the  $d_{xy2}$  band.

For STO, the SOC energy scale is  $\lambda \sim 25$  meV

$$H_{SOC} = \lambda \hat{\mathbf{L}} \cdot \hat{\boldsymbol{\sigma}} \quad (2)$$

$\hat{\boldsymbol{\sigma}}$  are the Pauli matrices and the angular momentum operator  $\hat{\mathbf{L}}$  is expressed in  $t_{2g}$  orbital space.  $L_x$ ,  $L_y$  and  $L_z$  are three of the eight Gell-Mann matrices which represent the SU(3) group. They describe an  $L = 1$  angular momentum.

$$L_x = \begin{pmatrix} 0 & 0 & 0 \\ 0 & 0 & i \\ 0 & -i & 0 \end{pmatrix} \quad L_y = \begin{pmatrix} 0 & 0 & -i \\ 0 & 0 & 0 \\ i & 0 & 0 \end{pmatrix} \quad L_z = \begin{pmatrix} 0 & i & 0 \\ -i & 0 & 0 \\ 0 & 0 & 0 \end{pmatrix} \quad (3)$$

The size of the OM term is  $\gamma_{OM} \sim 20$  meV ( $\sim 5$  meV) for the  $d_{xy1}$  ( $d_{xy2}$ ) band [61]. With our choice of parameters, we get a very good agreement between the tight binding and ARPES band structures [62].

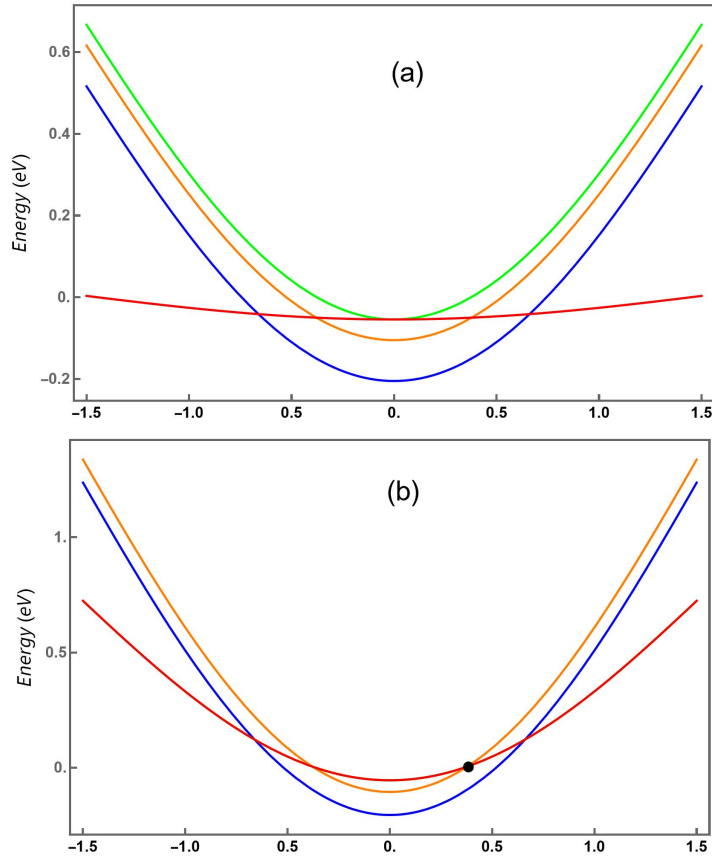


**Figure 1.** Band dispersions for zero OM and SOC along (a) [100] and (b) [110]. Horizontal scale,  $k_x$  (case (a)) and  $k=k_x=k_y$  (case (b)). Blue : lowest energy  $d_{xy}$  band. Orange : second lowest energy  $d_{xy}$  band. Red :  $d_{yz}$  band. Green :  $d_{xz}$  band. The lowest energy of a three band crossing corresponds to the intersection of the second lowest energy  $d_{xy}$  band with the  $d_{yz}$  and  $d_{xz}$  bands (black dot in (b)). The chemical potential  $\mu=0$  [41].

When spin orbit and orbital mixing terms are included, the “triple” Dirac point evolves into a regular Dirac point at  $\Gamma_{DP}$  and a split off branch. We show a zoom of the bands in the first quadrant of the BZ, in the vicinity of  $\Gamma_{DP}$ , along [110] Figure 2 (a) and along  $\Delta$ , the axis parallel to  $[\bar{1}10]$  passing through  $\Gamma_{DP}$  Figure 2 (b). We notice the tilting of the axis and the evolution of the angle of the cone between [110] and  $\Delta$ . Figure 2 (b) clearly shows the band inversion occurring in the vicinity of  $\Gamma_{DP}$ . The energy at  $\Gamma_{DP}$  is a fraction of a meV below the Fermi energy. Figure 2 (b) then suggests that the chemical potential falls within the gap of the inverted bands. Its magnitude varies as one moves around  $\Gamma_{DP}$ , but it was shown that a stable topological state is present.

As we indicated previously, a second quartet of tilted Dirac points is found at higher band filling due to the crossing of the  $d_{xy1}$  band with  $d_{yz}$ ,  $d_{xz}$  along [110] and  $[\bar{1}10]$ .

Topological manifestations are the occurrence of spin winding around Fermi energy contours [6, 62–64]. In practice, one may take advantage of this winding to generate an Inverse Edelstein, spin to charge current density response. The efficiency of the process for the 2DES is evaluated by measuring the ratio between the charge current in response to a spin density. This ratio,  $\lambda_{IEE}$  has the dimension of a length. At low temperature, the conversion between spin density and

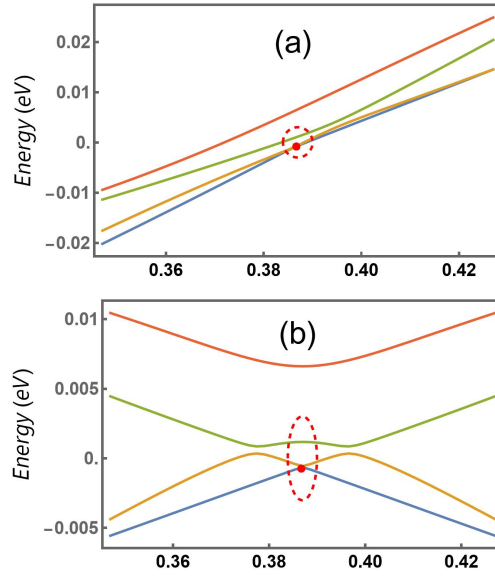


**Figure 2.** Zoom of the band structure with SOC and OM near  $\Gamma_{\text{DP}}$  along (a)  $[110]$  and (b) along  $\Delta$ , the direction parallel to  $[\bar{1}10]$  passing through  $\Gamma_{\text{DP}}$ . The red dot corresponds to  $\Gamma_{\text{DP}}$  and the red dashed circle or ellipse highlights the band geometry in its vicinity.  $\mu = -0.0007$  eV; the filling is  $10^{14} \text{ cm}^{-2}$  [41].

charge current for STO [62, 65] is at least three times larger than that observed in other studied systems, as shown in Table 1 [12, 66].

**Table 1.** Efficiency of the spin to charge conversion.

Compound	W	Pt	Ag/Bi	$\alpha$ -Sn	HgTe	LAO/STO	STO
$\lambda_{IEE}$ (nm)	<1	<1	0.08	2.1	2	6	$\pm 20$

Once again, this winding is the result of the combined SOC and OM parts of the hamiltonian. It produces an Edelstein effect when a charge current flows through a sample. The spin current may be converted back to a charge current in a non local Hall bar setup. The Edelstein tensor  $\kappa_{\alpha\beta}$  is the spin density response along the  $\beta$  axis to an electric field applied along the  $\alpha$  axis. In the following  $\kappa_{xy}$  represents the Edelstein coefficient [42].

$$\kappa_{xy}(\mu) = \frac{e}{N_k a^2} \sum_{k,v} \tau_v(k) v_{vx}(k) \langle S_y \rangle_v(k) \delta(E_v(k) - \mu) \quad (4)$$

The summation is over the band index  $v$ , and  $k$  the wavevector.  $\frac{1}{N_k}$  is a normalization factor which depends on the  $k$ -mesh  $\frac{1}{N_k a^2} \sum_k \approx \iint_{\text{BZ}} \frac{d_2 k}{4\pi^2}$ . For band  $v$ ,  $\tau_v$  is the scattering time,  $v_{vx}$  the velocity along the  $x$  axis,  $\langle S_y \rangle_v$  the expectation value of the dimensionless spin operator along the  $y$  axis and  $E_v$  is the energy. A priori these quantities depend on  $v$  and  $k$ . We relax the constraint on the scattering time and assume that it is a constant  $\tau^v(k) = \tau_0$ . This expression holds for zero temperature but it is readily extended to non-zero temperature by replacing the  $\delta$  function with a thermally broadened version. We transform Eq. 4 into a Fermi surface integral

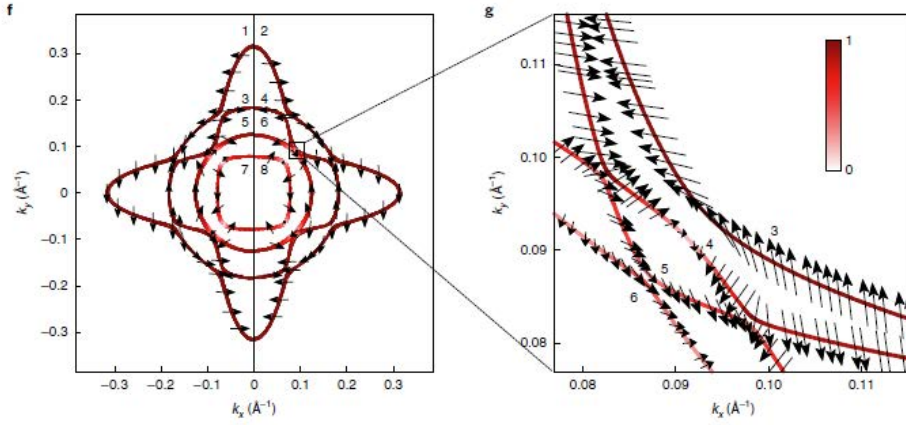


**Figure 3.** Spin winding at the Fermi energy for the Al/STO interface [62].

$\kappa_{xy}(\mu) = \sum_{\nu} \int \frac{d^2k}{4\pi^2} F_{\nu}(k) \delta(E_{\nu}(k) - \mu)$  with  $F_{\nu}(k) = \tau_0 \langle v_x \rangle_{\nu}(k) \langle S_y \rangle_{\nu}(k)$ . Using the symmetries of the system and Stokes theorem, the Edelstein coefficient  $\kappa$  is expressed as

$$\kappa(\mu) = \frac{e\tau_0}{2\pi\hbar} \sum_{\nu} \iint_{BZ} d_2k f_{\nu k}(\mu) (\vec{\nabla}_k \times \langle \vec{S} \rangle_{\nu}) \cdot \vec{z} \quad (5)$$

( $f_{\nu k} = \frac{1}{\exp\{(E_{\nu}(k) - \mu)/k_B T\}}$  is the Fermi distribution of band  $\nu$ ). Eq. (5) highlights the deep connection between spin winding (spin textures) and the Edelstein effect [42]. The existence of the OM term enhances the response. Indeed, close to  $\Gamma$ ,  $\mathcal{H}_{OM} = 2\gamma_{OM} a (\hat{L} \times \vec{k}) \cdot \vec{z}$  which is a linear Rashba-like form for  $\hat{L}$  ( $a$  is the lattice parameter). These spintronic effects have been experimentally observed in Al/STO and LAO/STO heterostructures [62, 65]. A further manifestation of topology is the existence of a spin Hall current driven by a charge current, and flowing in the in-plane direction perpendicular to the applied charge current [67, 68]. The Rashba-like form of the OM term close to  $\Gamma$  suggest that orbital winding is also present. We will return to this remark in the next section where we investigate the (111) geometry [66, 69].

### 3. Topology in the (111) orientation

When the heterostructure is grown along the (111) orientation, the stacking on the STO side consists of alternating Ti and SrO<sub>3</sub> planes. Figure 4 shows consecutive (111) Ti planes. Considering only Ti planes, viewed from the [111] direction, it is easy to see that there are three different types of Ti ions, “red” in the first layer, “blue” in the second, and green in the third. Then, the sequence repeats itself in the fourth and subsequent layers. A two-dimensional projection of the stacking, shown in the right panel of Figure 4, evidences a face centered honeycomb lattice. Experimental studies of this interface reveals the existence of a few nanometers thin, confined 2DES, on the STO side of the interface such that carriers move in an atomic honeycomb background [70–72].

In order to study the topological properties of this (111) interface, we construct the model tight binding hamiltonian which includes the appropriate energy terms [73–75]. Since carriers move between Ti sites, we hereafter focus on Ti layers. Hops between neighboring Ti have the largest amplitude, denoted by  $t$  ( $\sim 1.6$  eV) and they involve two consecutive layers. Figure 5 compares the electronic energies of the 2DES when we take into account all three layers of the stacking sequence or simply include two.



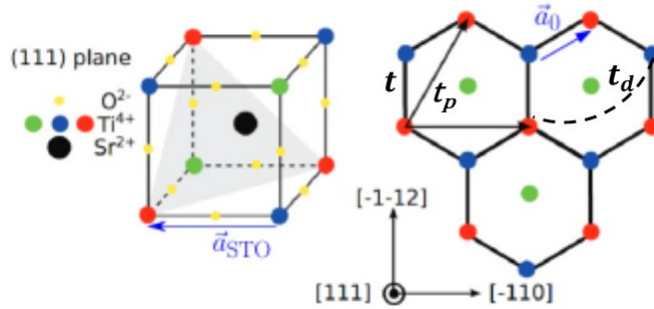


**Figure 4.** STO side, just below the (111) LAO/STO interface. Left: cubic lattice cell the corners of which are occupied by  $\text{Ti}^{4+}$  ions. The gray areas indicate planes normal to the [111] direction. Right: projection onto (111) planes. Two layers of  $\text{Ti}^{4+}$  ions (blue and red) form a honeycomb lattice, where the two triangular sublattices are displaced by the vector  $\vec{a}_0$ . ( $a_{\text{STO}} = 3.905\text{\AA}$  and  $a_0 = \sqrt{2/3}a_{\text{STO}}$ ). Hopping amplitudes between Ti sites belonging to two consecutive layers are  $t$  for nearest neighbors and  $t_d$  for next nearest neighbors (represented by a dashed line).  $t_p$  is the hopping between Ti sites belonging to the same layer.

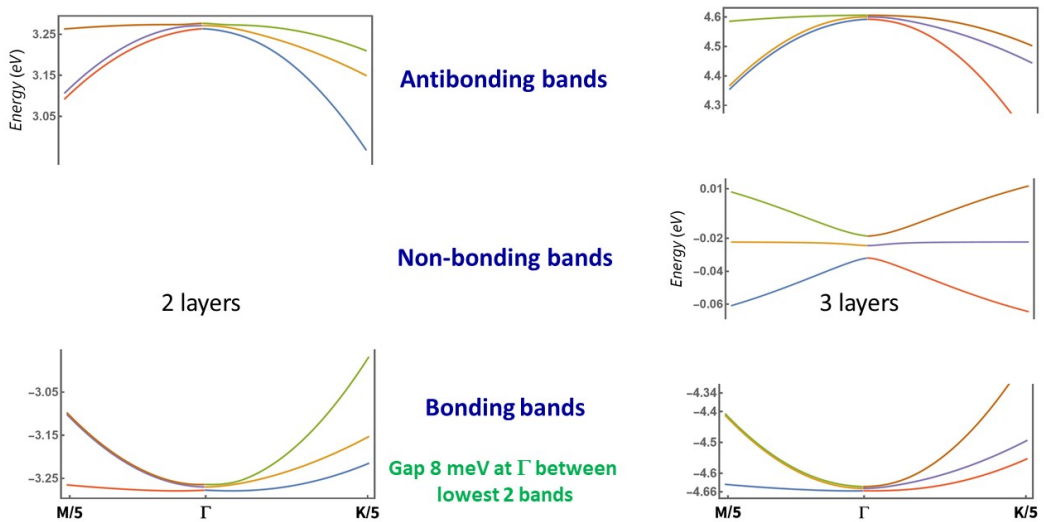


**Figure 5.** Comparison between the bilayer (left) and trilayer (right) tight-binding models [76].

In the former case, we have bonding, non bonding and antibonding bands. Bonding and antibonding states stem from hops between two consecutive Ti planes, say red and blue, non bonding states from hops between the first and third layer, say red and green. In the latter case, we only get bonding and antibonding bands. In either case, the energy separation between two consecutive groupings is several eV. ARPES studies indicate that the Fermi energy lies very close to the bottom of the lowest grouping, i.e within the bonding bands. Consequently we only consider two layers to describe the carrier motion parallel to the interface. This does not mean that the 2DES is confined to two layers. As explained previously, motion in the direction perpendicular to the interface is quantized. The extension of the wavefunction along [111] is on the order of 3 nm and this value gives an estimate of the thickness of the 2DES [72]. We also note that, along [111], confinement affects the three  $t_{2g}$  orbitals equally, so that the bonding and antibonding bands would both be energy degenerate at  $\Gamma$  if only kinetic terms were present. This property differentiates the (001) and (111) interfaces. Due to the directional character of the  $t_{2g}$  orbitals, Ti-Ti hopping amplitudes along the sides of the hexagons in Figure 4 (right panel) depend on the nature of the orbital. We introduce a  $t_{2g}$  basis  $|d_{\alpha\sigma}^i\rangle$ .  $i = 1, 2$  labels the Ti layer (red, blue),  $\alpha = 1, 2, 3$  identifies the orbital ( $1 \equiv yz$ ,  $2 \equiv xz$ ,  $3 \equiv xy$ ) and  $\sigma = \uparrow, \downarrow$  denotes the spin. The kinetic part is block diagonal in spin and orbital subspaces. The structure of the blocks in layer subspace  $|d_{\alpha\sigma}^1\rangle, |d_{\alpha\sigma}^2\rangle$  is given by

$$H_{\text{kin}_{\alpha\sigma}} = \begin{pmatrix} 0 & \varepsilon_{\alpha\sigma} \\ \varepsilon_{\alpha\sigma}^* & 0 \end{pmatrix} \quad (6)$$

where

$$\begin{cases} \varepsilon_{1\sigma} = -t \left\{ \exp(ik_y) + \exp \left[ i \left( \frac{\sqrt{3}}{2} k_x - \frac{1}{2} k_y \right) \right] \right. \\ \quad \left. - t_d \exp \left[ -i \left( \frac{\sqrt{3}}{2} k_x + \frac{1}{2} k_y \right) \right] \right\} \\ \varepsilon_{2\sigma} = -t \left\{ \exp(ik_y) + \exp \left[ -i \left( \frac{\sqrt{3}}{2} k_x + \frac{1}{2} k_y \right) \right] \right. \\ \quad \left. - t_d \exp \left[ i \left( \frac{\sqrt{3}}{2} k_x - \frac{1}{2} k_y \right) \right] \right\} \\ \varepsilon_{3\sigma} = -t \exp \left( -\frac{i}{2} k_y \right) \times 2 \cos \left( \frac{\sqrt{3}}{2} k_x \right) - t_d \exp(ik_y) \end{cases} \quad (7)$$

A good fit to the ARPES data is obtained for  $t = 1.6$  eV,  $t_p = 0$  and  $t_d = 0.07$  eV (see right side of Figure 4).  $k_x, k_y$  are dimensionless quantities (momentum  $\times a_0$ ) and  $x, y$  refer to the  $[\bar{1}10]$  and  $[\bar{1}\bar{1}2]$  directions respectively. Note that we chose the origin of the coordinate system at  $\Gamma$  and that the  $\varepsilon$  coefficients are spin independent.

While the crystal symmetry of STO is cubic in the bulk, it is trigonal at the interface. This produces an extra crystal field splitting affecting the  $t_{2g}$  orbitals. For this particular interface, the  $a_{1g}$  state is lower in energy than the  $e_{\pm g}$  ones. The corresponding hamiltonian is diagonal in layer and spin subspaces. In orbital subspace  $|d_{1\sigma}^i\rangle, |d_{2\sigma}^i\rangle, |d_{3\sigma}^i\rangle$ , it reads

$$H_{\text{trig}_{i\sigma}} = d \begin{pmatrix} 0 & 1 & 1 \\ 1 & 0 & 1 \\ 1 & 1 & 0 \end{pmatrix}, \quad (8)$$

where  $d = -3$  meV [77]. In order to account for the different value of the electrostatic potential in layers 1 and 2, we assign a spin independent site energy  $-V$  to layer 1,  $+V$  to layer 2 ( $V=50$  meV) to all three Ti orbitals.

A crucial contribution to the tight binding hamiltonian comes from the OM term. We discussed its origin in Section 1 and saw its relevance for the topological properties of the (001) oriented interface. For the (111) interface, this OM term plays an important role as well. It is spin independent and it results from electron hops between nearest neighbor Ti sites such that the

orbital character at the starting point is different from that at the end point. The two orbitals that are coupled belong to two different layers. Its expression is

$$\text{HOM}_\sigma = \gamma \begin{pmatrix} 0 & i\Delta_k & -iA_k \\ -i\Delta_k & 0 & iB_k \\ iA_k & -iB_k & 0 \end{pmatrix}, \quad (9)$$

where  $\gamma = 40$  meV. The left panel of Figure 4 shows that the symmetry operations consist of a rotation about the [111] axis of the cube such that  $1 \rightarrow 3, 2 \rightarrow 1, 3 \rightarrow 2$  (for the  $\alpha$  index) and a (110) mirror plane which exchanges 1 and 2. The counterpart in  $(\mathbf{k}_x, \mathbf{k}_y, \mathbf{k}_z \equiv [111])$  space is a  $\frac{2\pi}{3}$  rotation about the center of the hexagon and a mirror plane ([111],  $[\bar{1}\bar{1}2]$ ) which changes  $k_x$  into  $-k_x$  and leaves  $k_y$  invariant. Performing these symmetry operations gives  $A_k(-k_x) = -B_k(k_x)$ ,  $\Delta_k(-k_x) = -\Delta_k(k_x)$ ,  $\Delta(\mathbf{k}') = A_k(\mathbf{k})$ ,  $A(\mathbf{k}') = B_k(\mathbf{k})$ ,  $B(\mathbf{k}') = \Delta_k(\mathbf{k})$ , where  $k'_x = -\frac{1}{2}k_x - \frac{\sqrt{3}}{2}k_y$  and  $k'_y = \frac{\sqrt{3}}{2}k_x - \frac{1}{2}k_y$ . Symmetry requires that  $A_k, B_k, \Delta_k$  go linearly to zero in  $\mathbf{k}$  at  $\Gamma$  and at the three  $M$  points. This allows one to unambiguously determine the expressions of  $A_k, B_k, \Delta_k$ .

$$\begin{cases} A_k = \sin\left(\frac{\sqrt{3}}{2}k_x + \frac{3}{2}k_y\right) \\ B_k = \sin\left(\frac{\sqrt{3}}{2}k_x - \frac{3}{2}k_y\right) \\ \Delta_k = -\sin(\sqrt{3}k_x) \end{cases} \quad (10)$$

In the small  $\mathbf{k}$  limit,  $\text{HOM}_\sigma = \gamma(\vec{\mathbf{L}} \times \vec{\mathbf{k}}) \cdot \vec{u}_{111}$ .  $\vec{u}_{111}$  is the unit vector in the [111] direction and  $\vec{\mathbf{L}}$  is the angular momentum operator in  $t_{2g}$  orbital space (see Eq. (3)). This form evokes an ‘‘orbital’’ Rashba interface hamiltonian (see section 1).

Next, we have the atomic spin-orbit term. Its expression was given in Eq. (2). Lastly we include Hubbard terms describing electron-electron interactions. When we discussed the kinetic terms pertaining to the (111) oriented 2DES we pointed out that the band structure of the 2DES describes the motion of the carriers parallel to the interface and that the motion perpendicular to the interface is quantized in the form of sub-band levels. The sequence of levels describes electrons with average vertical positions further and further removed from the interface. The effective Hubbard energy pertaining to carriers located a depth  $z$  is  $\sim U\psi(z)^4$  where  $U$  is the value at the interface and  $\psi(z)$  is the  $z$ -dependent part of the eigenfunction of the quantized level. This function decays exponentially with  $z$ . Experiments performed on the (111) LAO/STO heterostructure evidence a group of bands close to the interface. Given the energy resolution of the technique (electron holography) one should also include a second group, very close to the Fermi level. The Hubbard interaction of the former group is denoted  $U_1$ , that of the latter group  $U_2$ . There is also an interaction  $U'$  between the two group akin to the inter-orbital term that is used in the Kanamori hamiltonian [78] which implements Hund’s rules.

We now turn to a discussion of the topological properties of the (111) oriented interface, in the metallic regime [79]. Generically, there are four time reversal symmetry invariant points in the hexagonal BZ. One is  $\Gamma$  and the other three are the  $M$  points, since  $2\vec{k}_M = \vec{0}$  modulo a reciprocal lattice vector. Hence the eigenfunctions of the hamiltonian are real at these point. Furthermore if we exchange the red and blue Ti sites, i.e layers 1 and 2, we observe that, for the bonding bands of interest, the sign is unchanged (reversed) at  $\Gamma$  (at  $M$ ). So we have an even parity at  $\Gamma$  and an odd parity at  $M$ . The spin-orbit interaction opens up a gap at  $M$  which protects the odd parity states. We note that the OM term is strictly zero at  $\Gamma$  and  $M$ . We expect a non trivial  $\mathbb{Z}_2$  topological index. This is indeed borne out in the computation of the eigenstates for strips that are infinite along  $x$  and finite in the  $y$  direction. They reveal the presence of edge states near  $M$ , as can be seen in Figure 6 which shows an array of extended bands. The array is due to the finite extent in the  $y$  direction which leads to a quantization of the energy levels. The conduction band states, which are relevant to the interface span an energy range  $\sim 3.25 - 7.25$  eV. We note the presence of

two particular bands in the spectrum, shown in red color. These bands touch the top and bottom boundaries of the array then, at the  $K$  points, split from the group of conduction bands and span the gap. These are the edge states that stem from the parity inversion. We plot the amplitude of the edge state wavefunction in the  $y$  direction at  $M$  first, then at  $K$  (Figure 7). It is apparent that the edge state is strongly localized near the boundary of the strip at  $M$  and that it is extended and has merged with conduction band states at  $K$ .

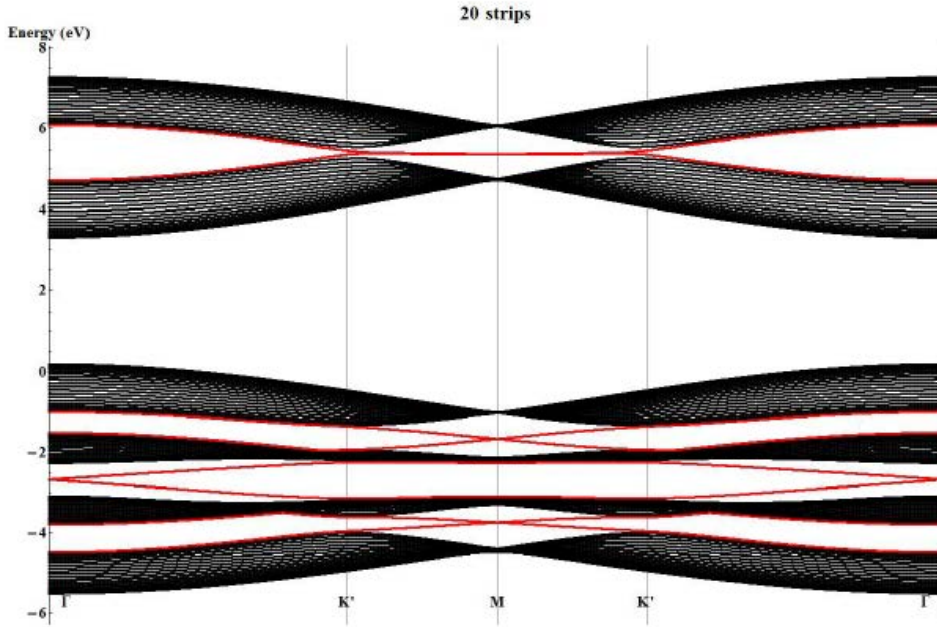


**Figure 6.** Band dispersion for a  $L \times \infty$  strip along a path  $\Gamma \rightarrow K \rightarrow M \rightarrow K' \rightarrow \Gamma$ . Bands drawn in black color represent extended states, in red color, edge states. The conduction band extends between 3.25 and 7.25 eV [79].

From an experimental perspective the chemical potential that one can tune with gating remains relatively close to the  $\Gamma$  point, so that it is not clear that one can reach this topological region.

A second instance leading to the emergence of a topological regime for this interface is when one applies a gate voltage. The influence of the Hubbard term can be qualitatively assessed within a Hartree-Fock (mean field) approach. In the framework of this approximation, the energies of the interacting system are given by the non-interacting single particle energies augmented by a factor  $U\langle n \rangle$  ( $\langle n \rangle$  is the expectation value of the site occupancy). This leads to a (rigid) upward energy shift of the band structure. By contrast for these interfaces, it is found that the existence of  $U$  and of a field dependent dielectric constant result in a downward shift of the second group of quantized levels and an upward shift of the first group, as the carrier density is increased. Such behavior underscores the lack of rigid band shifts for these 2DES [32, 80–82]. This leads to the configuration shown in Figure 8.

This situation is similar to the scenario that we discussed for the (001) interface. Here too, the topological crossing occurs within the conduction band and its manifestations are limited to a very narrow range of values of the chemical potential.

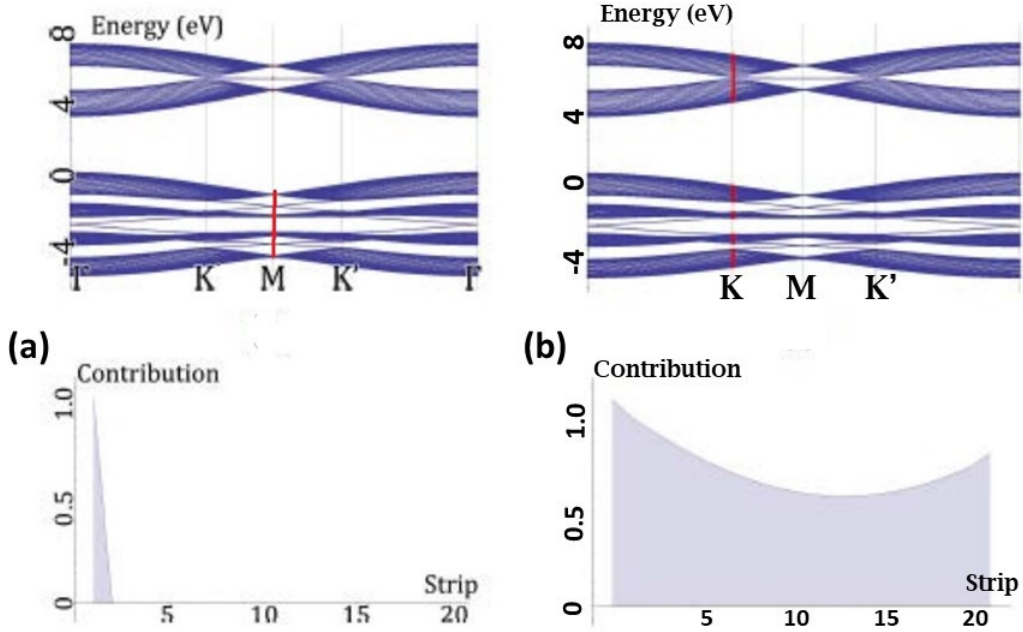


**Figure 7.** (a) Amplitude of the edge state wavefunction versus  $y$  at an  $M$  point (indicated by the red vertical bar in the energy diagram at top). (b), Amplitude of the edge state wavefunction versus  $y$  at a  $K$  point (indicated by the red vertical bar in the energy diagram at top). The dimensionless strip width is  $L = 20$ . Zero corresponds to the edge of the strip, twenty to the opposite edge. Adapted from [79].

While the two cases that we just discussed involve finite values of the momenta, we now unveil the topological states that are present near  $\Gamma$  and argue that they have spintronic consequences. Our tight binding modeling of the (111) 2DES is such that that each quantized group of bands contains twelve dispersions, six bonding and six antibonding, separated in energy by several eV. Experimentally, only the bonding bands are partially filled so we hereafter focus on that subspace. At  $\Gamma$ , the OM term is zero and we have three doubly degenerate energy levels (due to time reversal symmetry). The energy separation between the two lowest levels is  $\sim 8$  meV and the chemical potential that is extracted from transport measurements falls within the gap. The area of the BZ that pertains to the (111) interface is such that  $|k_x|, |k_y| \leq 0.5$ . We proceed to demonstrate that the interplay of multi-orbital kinetic terms, of angular momentum and spin-orbit interaction leads to Berry curvature and quantum metric effects in the (111) 2DES.

### 3.1. Fermi surface anisotropy driven Berry curvature

As a preliminary step, we give a simple example showing how a Fermi surface anisotropy can be the source of a Berry curvature. We consider a two-orbital problem, where orbitals are denoted by 1 and 2. We introduce Pauli matrices  $\tau_x, \tau_y, \tau_z$  in orbital space such that 1(2) corresponds to the  $+1$  ( $-1$ ) eigenstate of  $\tau_z$ . In  $k$  space, the kinetic energy of an electron occupying orbital 1 is

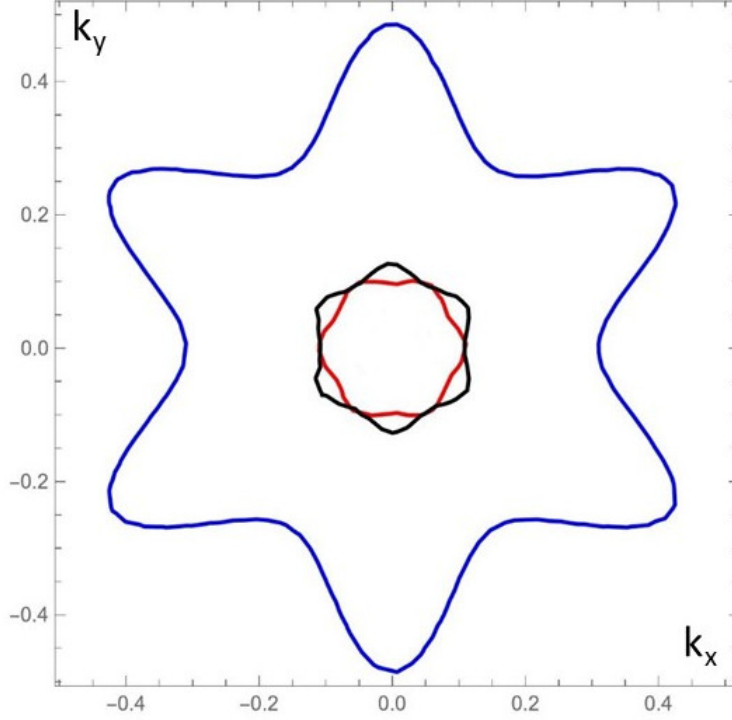


**Figure 8.** Momentum dispersion curve at the Fermi energy for the first two sets of quantized bands. In blue and red, first set (only two bands are shown for clarity), in black the lowest energy band of the second quantized group. Red and black bands touch at the Fermi level.  $k_x$  and  $k_y$  are dimensionless quantities (momentum  $\times a_0$ ).

$e_1 = ak_x^2 + bk_y^2$  and that of an electron occupying orbital 2  $e_2 = bk_x^2 + ak_y^2$ . An orbital mixing term promotes hops between orbitals 1 and 2. The hamiltonian of this model reads

$$\mathbf{H} = \begin{pmatrix} e_1 & -i\alpha(k_x - ik_y) \\ i\alpha(k_x + ik_y) & e_2 \end{pmatrix}, \quad (11)$$

If we define  $e_0 = \frac{1}{2}(e_1 + e_2)$ ,  $g(\mathbf{k}) = \frac{1}{2}(e_1 - e_2)$  and  $\tau_0$  as the unit matrix, we express  $\mathbf{H}$  as

$$\begin{aligned} \mathbf{H} &= e_0\tau_0 - \alpha\mathbf{u}_z \cdot (\boldsymbol{\tau} \times \mathbf{k}) + g(\mathbf{k})\tau_z \\ &= e_0\tau_0 + \mathbf{d}(k) \cdot \boldsymbol{\tau} \end{aligned} \quad (12)$$

This  $2 \times 2$  hamiltonian gives rise to two bands  $e_+$  and  $e_-$ . Their Berry curvature  $\Omega$  points along  $\mathbf{u}_z$  and is given by

$$\Omega_{\pm}^z = \mp \frac{1}{2} \alpha^2 \frac{g(\mathbf{k})}{(g(\mathbf{k})^2 + \alpha^2 \mathbf{k}^2)^{3/2}} \quad (13)$$

So the anisotropy of the bands, characterized by  $g(\mathbf{k})$  and the orbital mixing, by  $-\alpha\mathbf{u}_z \cdot (\boldsymbol{\tau} \times \mathbf{k})$  produce a finite Berry curvature.

### 3.2. Orbital textures as a source of Berry curvature

Here, we undercore the fact that the interplay of the trigonal crystal field Eq. (8), of the OM part Eq. (9) and of the kinetic terms Eq. (6) also gives rise to topological effects. The layer potential energy  $V$  only shifts the spectrum rigidly, so that we omit it in the present discussion. A convenient orbital basis is one which diagonalizes the trigonal crystal field hamiltonian. The rotation matrix connecting the orbital and trigonal bases is

$$P = \begin{pmatrix} -\frac{1}{\sqrt{2}} & -\frac{1}{\sqrt{6}} & \frac{1}{\sqrt{3}} \\ \frac{1}{\sqrt{2}} & -\frac{1}{\sqrt{6}} & \frac{1}{\sqrt{3}} \\ 0 & \frac{2}{\sqrt{6}} & \frac{1}{\sqrt{3}} \end{pmatrix} \quad (14)$$

In terms of Gell-Mann matrices,

$$\mathbf{H}_{\text{trig}} = d\Lambda_8 \quad (15)$$

We pointed out that the bonding bands were relevant to the experimental situation which simplifies the tight binding modeling of the (111) interface. So we project the kinetic part of the hamiltonian onto the bonding sub-space. Since we are considering here the impact of topology on the orbital states, we turn off spin-orbit and omit the spin index. In the trigonal basis Eq. (14) The kinetic hamiltonian (see Eq. (7)) is

$$\mathbf{H}_{\text{kin}} = \frac{\varepsilon_1 + \varepsilon_2 + \varepsilon_3}{3} I_3 + \frac{\varepsilon_1 + \varepsilon_2 - 2\varepsilon_3}{6} \Lambda_3 + \frac{\varepsilon_1 - \varepsilon_2}{2\sqrt{3}} \Lambda_1 - \frac{\varepsilon_1 - \varepsilon_2}{2\sqrt{6}} \Lambda_4 - \frac{\varepsilon_1 + \varepsilon_2 - 2\varepsilon_3}{3\sqrt{2}} \Lambda_6 \quad (16)$$

Lastly, the OM part takes the form

$$\mathbf{H}_{\text{OM}} = B'_k L_x + A'_k L_y + \Delta'_k L_z \quad (17)$$

where the angular momentum matrices  $L_x, L_y, L_z$  have the same expression in the trigonal basis as in the orbital basis (see Eq. (3)) and

$$\begin{cases} A' = -\frac{1}{\sqrt{6}}(A + B - 2\Delta) \\ B' = \frac{1}{\sqrt{2}}(A - B) \\ \Delta' = \frac{1}{\sqrt{3}}(A + B + \Delta). \end{cases} \quad (18)$$

where  $A, B, \Delta$  have been defined in Eq. 10. The full hamiltonian ( $6 \times 6$  matrix) is

$$\mathbf{H} = \begin{pmatrix} \mathbf{H}_{0\text{trig}} & \mathbf{H}_{\text{kin}} + \mathbf{H}_{\text{OM}} \\ \mathbf{H}^*_{\text{kin}} + \mathbf{H}_{\text{OM}} & \mathbf{H}_{0\text{trig}} \end{pmatrix}, \quad (19)$$

where  $\mathbf{H}_{0\text{trig}}$  is the trigonal crystal field matrix expressed in the trigonal basis (hence diagonal, with entries  $d, d, -2d$ ).

The Berry curvature is obtained once we know the eigenvalues and eigenfunctions of  $\mathbf{H}$

$$\Omega_v^z(k) = -2\text{Im} \left[ \sum_{\chi \neq v} \frac{\langle v_k | \hat{v}_x(k) | \chi_k \rangle \langle \chi_k | \hat{v}_y(k) | v_k \rangle}{(E_v(k) - E_\chi(k))^2} \right] \quad (20)$$

Where  $|v_k\rangle, |\chi_k\rangle$  are eigenvectors of the hamiltonian. The velocity operators are given by  $\hat{v}_\beta(k) = \partial_{k_\beta} \mathbf{H}(k)$ . The numerical solution of Eq. (20) gives a finite value of the Berry curvature near  $\Gamma$ . Figure 9, which pertains to the lowest energy bonding band, shows that  $\Omega_v^z(k)$  is odd in  $k_x$  and even in  $k_y$ . In the small  $\mathbf{k}$  limit, the Fermi contours are circles, such that the angular average of  $\Omega_v^z(k)$  over these contours is zero.

Inspection of the terms in the sum contributing to the Berry curvature, for the lowest energy band, reveals that the dominant ones come from interband virtual transitions within the bonding group. Indeed, the gap in that group is on the order of  $3d \sim 10$  meV whereas the bonding-antibonding gap is  $\sim 4t$ . We note however that the Berry curvature can only be non zero if the OM term is present. But we further observe that we only get a finite value if at least one

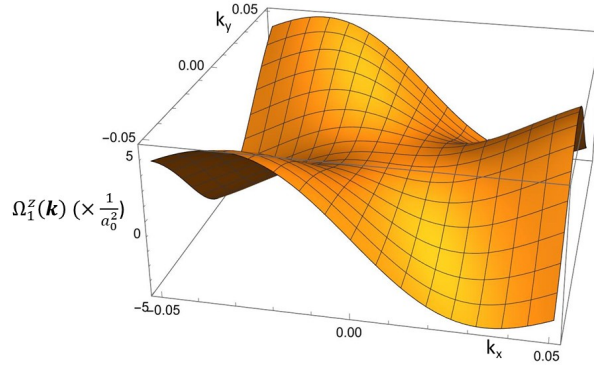


**Figure 9.** Berry curvature of lowest energy bonding band in a small range of values of  $\mathbf{k}$  near  $\Gamma$ .  $k_x$  and  $k_y$  are dimensionless quantities (momentum  $\times a_0$ ).

of the following two conditions is met (i) the chemical potential is such that the band structure is anisotropic in  $k$  space or/and (ii) the eigenfunctions of  $H(k)$  are linear superpositions of  $a_{1g}$  and  $e_{\pm g}$  wavefunctions which include *both* bonding and antibonding groups. One may understand (ii) as due to the fact that the anomalous part of the velocity operator mixes the two groups, more precisely the parity of the state, since the bonding bands have even parity and the antibonding bands have odd parity. Close to  $\Gamma$ , the band dispersions are isotropic in  $k$  space, but nevertheless criterion (ii) is satisfied. If we project  $H$  onto the bonding space, its eigenfunctions will only contain components of the same parity and the Berry curvature will be zero. So, while the low energy modeling captures most of the physics, it falls short of describing Berry curvature effects.

As we pointed out in Section 2, the finite value of the Berry curvature signals the existence of orbital textures. Close enough to  $\Gamma$ , the Fermi contour of the lowest bonding energy branch in the BZ is a circle, but as discussed in the previous paragraph wavefunctions are linear combinations of bonding and antibonding eigenstates. We plot the expectation value over the lowest energy wavefunction of the two dimensional vector  $\vec{L}_{in} = (L_x, L_y)$  around the Fermi contour as well as the sign of the expectation value of  $L_z$  over the lowest energy wavefunction. This is shown in Figure 10.

$\vec{L}_{in}$  winds around the Fermi contour, similarly to what is found in a (spin) Rashba case and gives a +1 winding number. Remarkably, the sign of  $L_z$  alternates around the Fermi circle. The amplitude (not shown) also varies and goes to zero at the boundary between positive and negative regions (“domain walls”).

Note that we chose a range of values of momenta such that the Fermi contours are circles, meaning that the dispersion is isotropic in  $k$  space. The topological properties derive from the entanglement of the orbital components of the wavefunction.

We may repeat the analysis for the experimentally relevant area of the BZ ( $|k_{Fx}|, |k_{Fy}| \sim 0.3$ ). The Berry curvature and orbital textures are the combined result of the Fermi surface anisotropy and of the orbital entanglement (Figure 11).

We noted above that the Berry curvature is odd in  $k_x$  and even in  $k_y$ , implying that the integral of  $\Omega_v^z(k)$  over an area of the BZ centered at  $\Gamma$  gives zero, but the integral of  $\frac{\partial \Omega_v^z(k)}{\partial k_x}$  is finite, giving rise to a Berry curvature dipole  $D$  parallel to  $k_x$  (BCD) [83–85].



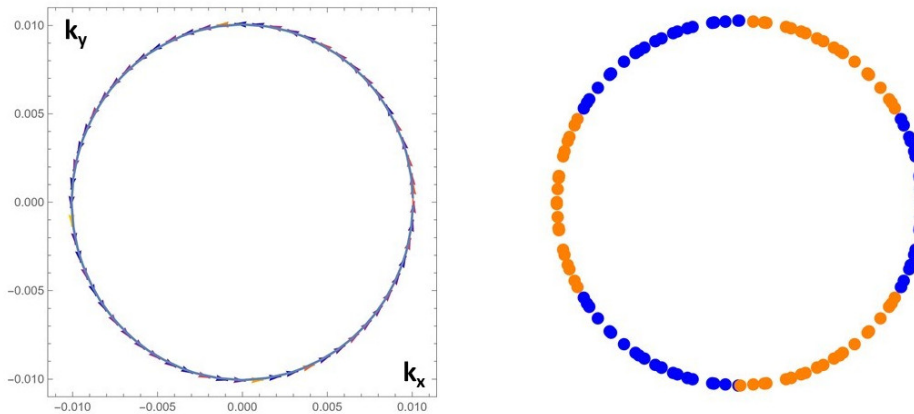


**Figure 10.** Left in-plane vector plot of the expectation value of  $(L_x, L_y)$  over the Fermi circle, close to  $\Gamma$ . Right sign of out-of-plane expectation value of  $L_z$  over the Fermi circle. Blue is positive, orange is negative. Note the  $C_3$  symmetry.  $k_x$  and  $k_y$  are dimensionless quantities (momentum  $\times a_0$ ).

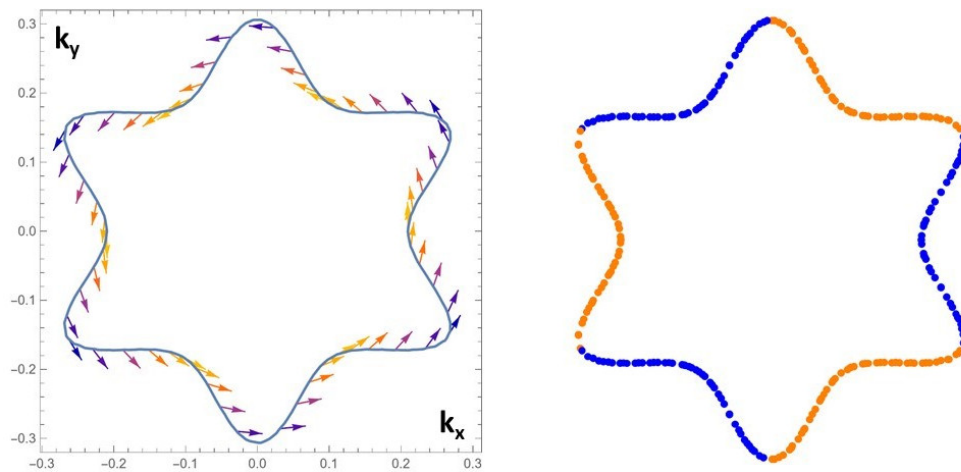


**Figure 11.** Left in-plane vector plot of the expectation value of  $(L_x, L_y)$  over the Fermi contour for the experimentally relevant value of the chemical potential (100 meV). Right sign of out-of-plane expectation value of  $L_z$  over the Fermi contour. Blue is positive, orange is negative. Note the  $C_3$  symmetry.  $k_x$  and  $k_y$  are dimensionless quantities (momentum  $\times a_0$ ).

$$D_{vx} = \frac{3\sqrt{3}}{8\pi^2} \int d_2k \frac{\partial \Omega_v^z(k)}{\partial k_x} f_{vk} \quad (21)$$

For (111) LaO/STO, with the tight binding parameters that we used, we find  $D_x \sim 0.02a_0$ . Note that we obtain a finite value even for the  $C_3$  and time reversal symmetric case, but only if the 6 antibonding bands of our 12 band model are included. In Ref. [84], the existence of an applied driving current still breaks the above symmetries and for small values of  $\sigma_S$ , the BCD is very small ( $\sim 1$  nm) but non-zero. In our model, only the lowest band is occupied, which corresponds to a range of fillings such that  $\sigma_S \sim 1$  mS, which has previously been explored [80, 81, 86]. If we increase the filling, more bands will get populated. When the bands that are 8meV higher in energy at  $\Gamma$  start getting occupied, the BCD reaches a value  $D_x \sim -1.6a_0$ , i.e is 80 times larger than that pertaining to the lowest energy band. Then, if we keep increasing the filling we find that the absolute value of  $D_x$  drops sharply. This evolution and the magnitude of the variation are clearly consistent with Lesne's et al. data [84].

Several experimental implications of these properties pertain to spintronic transport [66, 87].

- An orbital Edelstein effect is expected, similar to the one that we introduced previously in Eq. (4). The expectation value  $\langle S_y \rangle_v$  is replaced by  $\langle L_y \rangle_v$ . The relaxation time,  $\tau_v$  is not the same as that pertaining to the spin case. Transport of angular momentum is a priori more sensitive to disorder (non magnetic impurities cause scattering). This could lead to an angular momentum accumulation at the edge of a Hall bar, detectable by Kerr effect.
- An orbital Hall conductivity, which is the counterpart of the spin Hall conductivity [67] discussed in Section 2. The intrinsic part of the orbital Hall conductivity is defined via the so-called orbital curvature (a variant of the Berry curvature):

$$\omega_v^z(k) = -2Im \left[ \sum_{\chi \neq v} \frac{\langle v_k | \hat{v}_x^z(k) | \chi_k \rangle \langle \chi_k | \hat{v}_y(k) | v_k \rangle}{(E_v(k) - E_\chi(k))^2} \right] \quad (22)$$

where the orbital velocity is  $\hat{v}_x^z = \{\hat{v}_x, \hat{L}_z\}$ .

The above form stems from the Kubo formalism in combination with the Streda formula. The total response of the model is then obtained by summing over all occupied states; the intrinsic part of the orbital Hall conductivity reads

$$\sigma_{xy}^z(\mu) = \frac{e}{\hbar} \frac{3\sqrt{3}}{8\pi^2} \sum_v \int d_2k f_{vk} \omega_v^z(k) \quad (23)$$

- A non-linear second harmonic Hall current due to the DC and AC part of the driving electric field respectively (see the experimental study by G. Tuvia et al. [88]).

$$\begin{aligned} j_{0y} &= \frac{1}{\hbar^2} \frac{e^3 \tau}{2} \vec{z} \times \vec{E}^* (D_x \cdot E_x) \\ j_y &= \frac{1}{\hbar^2} \frac{e^3 \tau}{2(1 + i\omega\tau)} \vec{z} \times \vec{E} (D_x \cdot E_x) \end{aligned} \quad (24)$$

These manifestations pertain to the orbital degree of freedom. When we “turn on” the atomic spin-orbit, there is an additional spin contribution to the previous quantities. However, since the angular momentum quantum number is  $L = 1$ , we expect the orbital part to produce larger effects.

### 3.3. Spin textures

When we include the atomic spin-orbit term (Eq. (2)) our tight-binding hamiltonian is a  $12 \times 12$  matrix. Spin is no longer a conserved quantum number, but owing to time reversal symmetry,

bands split into Kramers doublets  $\pm$  such that  $E_+(\mathbf{k}) = E_-(-\mathbf{k})$ . In addition to the previously described orbital textures, we also get spin textures. In particular, the out of plane winding that we find nicely matches the experimental one, both for LAO/STO(111) [89] and for KTO(111) [90].

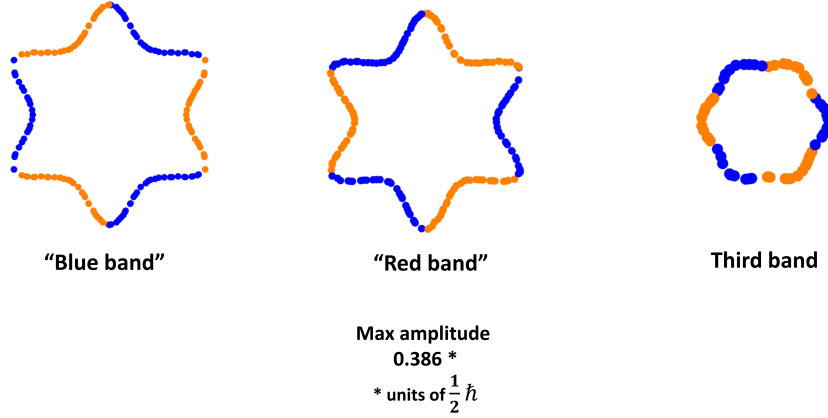


**Figure 12.** Sign of the out-of-plane expectation value of  $S_z$  over the Fermi contour for the experimentally relevant value of the chemical potential (100 meV) and for the first three energy bands. Blue is positive, orange is negative. Note the  $C_3$  symmetry. See Figure 11.

The energy difference of the lowest band at  $\Gamma$ , when spin-orbit is included and when it is not, yields an estimate of the out-of-plane texture strength. We find that it is  $\sim 1$  meV. Similarly, the shift of the energy minimum provides a determination of the in-plane Rashba spin textures energy scale,  $\sim 5$  meV.

### 3.4. Superconductivity and topology

In this section, we discuss two implications of the band topology pertaining to the superconducting instability of the (111) interface [76]. One relates to the Berry curvature that we obtained and one to the quantum metric which we introduce below. It has been shown that the Berry curvature reduces the pairing strength and transition temperature of a multiband system described by *isotropic* band dispersions [91]. This is a generic finding for a BCS type of instability with a pure, even or odd parity of the order parameter. The Berry curvature dipole, on the other hand, only affects the superconducting instability if the pairing potential has a mixed even-odd symmetry. For the situation that we are describing, the Fermi contour is anisotropic so that the above conclusions do not necessarily apply. Qualitatively, one may nevertheless surmise that they remain valid, since the dispersion is isotropic whenever the chemical potential is close to the lowest energy band bottom. Anisotropy sets in upon increasing the Fermi energy so that an adiabatic continuation is a plausible assumption. A second manifestation of the band topology on the superconducting instability involves the quantum metric  $g$ , the real part of the quantum geometric tensor  $Q$  [92–94].

$$Q_{\alpha\beta}^n = \langle \partial_\alpha n | (\mathbb{1} - |n\rangle \langle n|) | \partial_\beta n \rangle = g_{\alpha\beta}^n - \frac{i}{2} \Omega_{\alpha\beta}^n, \quad (25)$$

( $\alpha, \beta$  are the  $k$  space coordinates and  $n$  denotes a band eigenvector). In two dimensions one obtains the expression of the superconducting transition temperature from the Berezinskii-Kosterlitz-Thouless (BKT) theory. It is linearly related to the superconducting carrier density, the

latter consisting of the sum of a conventional and a geometric contribution [95]. For a parabolic band and an s-wave BCS superconductor the conventional part at  $T = 0$  is directly proportional to the chemical potential  $\mu$  (which is much larger than the superconducting gap). The geometric part involves an integral where the integrand contains  $g_{\alpha\beta}^n$ . Transport measurements of the 2DES in LAO/STO (111) indicate that  $\mu$  is close to the energy of the lowest band bottom. Owing to the Rashba-type two-fold degeneracy of that band at  $\Gamma$ ,  $g_{\alpha\beta}^n$  is sharply peaked in a very narrow range of the BZ around  $\Gamma$

The implication of this fact is that for increasing values of  $\mu$  the conventional part of the “superfluid” density tends to dominate. The influence of the geometric part is only felt for small values of  $\mu$ . This is in contrast to the case of twisted bilayer graphene or several transition metal dichalcogenides where the presence of flat bands quenches the conventional part and only leaves the geometric one [96]. Figure 13 shows the evolution of the conventional and geometric “ $T_{BKT}$ ” versus  $\mu$ . “ $T_{BKT}^{conv}$ ” is obtained when we only consider the conventional superfluid weight and “ $T_{BKT}^{geom}$ ” when we only consider the geometric superfluid weight [94, 95]. For  $\mu > 0.5$  meV, the conventional contribution dominates.

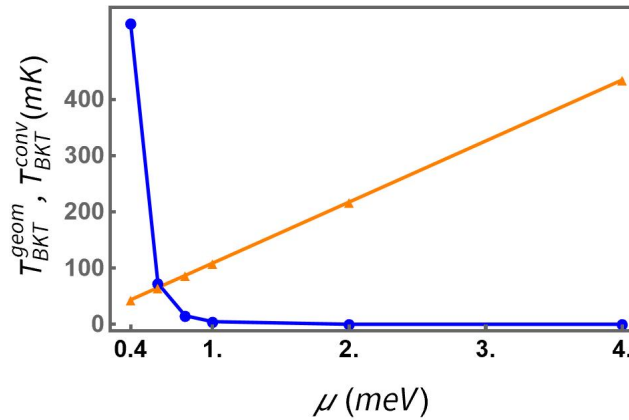


**Figure 13.** The conventional (orange) and geometric (blue) contributions to  $T_{BKT}$  versus  $\mu$ .

For a rigid band dispersive system, an increase in the carrier concentration  $n$  generically leads to an increase in the chemical potential (for a 2D parabolic band, the two quantities are linearly related). For perovskite based interfaces, the situation is more complicated. The experimental technique that is used to change the carrier concentration is gating. Doing so modifies the electric field profile at the interfaces which in turn impacts the dielectric constant and the mobility. The magnitude of these effects depends on the location of the carriers relative to the interface. Their average position is different for each quantized level of the 2DES and for the various eigenstate of a given sub-band. As one gates the heterostructure, the positions of the bands shift relative to one another. Coulomb interactions also modify the relative positions between bands. This is because Hubbard interactions are largest for sub-bands positioned close to the interface and between quantized levels that have smaller energy separations. It has also been argued that the anisotropic shape of the Fermi contours may impact the determination of  $n$  since the Hall number no longer gives access to  $n$  in the low magnetic field limit. So the correspondence between the applied gate voltage  $V_g$ , the carrier concentration and  $\mu$  is not a simple one.

In order to record a reproducible evolution of physical quantities with gating, experimental plots use the sheet conductance as the tuning parameter. Analysis of transport data for the

LAO/STO (111) interface indicate that the dependence of  $\mu$  on the sheet conductance  $\sigma$  shows a non monotonic behavior (Figure 14).

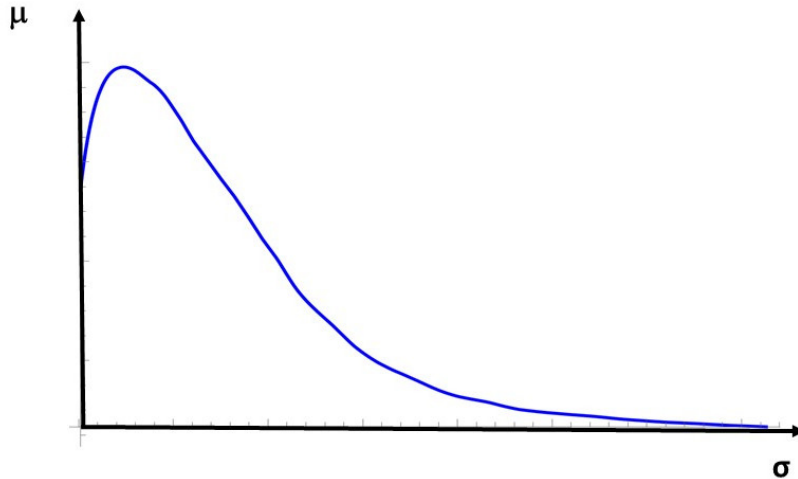


**Figure 14.** Sketch of the  $\mu$  versus  $\sigma$  profile.

At the lower end of the conductance range where superconductivity is observed,  $\mu$  is on the order of 1 meV, i.e the instability is dominated by the conventional contribution. As  $\sigma$  increases, so does  $\mu$  up to a maximum value which also corresponds to the maximum superconducting  $T_{BKT}$ . Beyond the maximum,  $\mu$  decreases as  $\sigma$  is further increased.  $T_{BKT}$  follows the same trend. However, for  $\mu \sim 0.5$  meV, the geometric contribution dominates and the observed  $T_{BKT}$  presents an upturn. Eventually, at very low  $\mu$ ,  $T_{BKT}$  goes down again. This leads us to propose a theoretical phase diagram giving  $T_{BKT}$  versus  $\sigma$ , displaying two regimes, one where the conventional response dominates (up to the so called optimal doping) and one where the geometric response is at play [76]. Each of these exhibits a dome, as is depicted in Figure 15 [80, 86, 97].

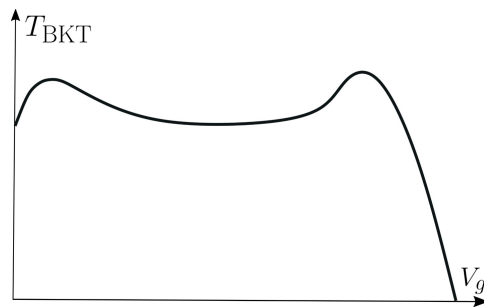


**Figure 15.** Plot of  $T_{BKT}$  versus  $V_g$ . The dome at lower (higher) values of  $V_g$  pertains to the conventional (geometric) regime [76].

## 4. Outlook

In this report, we showcased the relevance of topology concepts for perovskite oxide heterostructures. We gave a brief overview of the significant body of work devoted to this topic and we presented results of our recent research on the LAO/STO (111) interface. These underscore the fact that orbital entanglement occurs whenever the energies of the three  $t_{2g}$  states are degenerate. For (001) interfaces, confinement impacts the out-of-plane orbitals more than the  $d_{xy}$  one. Bands have an almost pure orbital character and the  $d_{xy}$  ones are lower in energy at  $\Gamma$ . Thus, the degeneracy occurs away from  $\Gamma$  and above the energy of the so-called Lifshitz transition (when the  $d_{xz}$  and  $d_{yz}$  bands become occupied). The crossing is of “Dirac type” (linear in-k energy dispersion in the vicinity of that point). For (111) interfaces, confinement impacts all three  $t_{2g}$  states equally. Consequently entanglement is present near  $\Gamma$  and the energy dispersion is quadratic in k. There are several aspects which we did not cover here. We summarily described a few spintronic implications, but left out aspects pertaining to the experimental setups allowing one to take advantage of these properties. While we showed that topological textures are hallmarks of these interfaces, we did not emphasize their impact on the symmetry of the superconducting order parameter. A fact that stands out is that the topological properties of the normal state drive a topological regime in the superconducting phase, with potential implications in terms on quantum computing. We indicated that confinement causes a quantized differentiation of the energy bands. This produces band crossings (avoided or not) upon gating, introducing further opportunities of getting topological textures. We limited the scope of our presentation to the LAO/STO (001) and (111) interfaces but the (110) case also deserves attention. Other types of perovskites, such as  $\text{LaTiO}_3$  (a Mott insulator in the absence of doping) or  $\text{KTaO}_3$  (which has a very large spin-orbit interaction energy) are clearly promising candidates. Lastly, we did not consider the late transition metal oxide perovskites, nickelates or cuprates, where the physics pertains to the  $e_g$  levels

## 5. A tribute to Gérard Toulouse

J’ai bien connu Gérard, pendant la période où il effectuait ses travaux de recherche au Laboratoire de Physique des Solides d’Orsay (LPS). Je démarrais alors une « thèse théorique de 3<sup>ème</sup> cycle » et j’étais intimidé et admiratif devant son attitude réservée, son savoir encyclopédique (au sens XVIII<sup>ème</sup> siècle du terme) et son humour « pince-sans-rire ». Il était une présence forte au sein du groupe théoriciens du laboratoire. Avec Pierre Pfeuty, il venait de publier une monographie sur la méthode du groupe de renormalisation qui était très en vogue à cette période. Il l’avait notamment appliquée à l’analyse du problème de l’impureté Kondo dans les métaux, donnant une description transparente de la physique de ce système. Un des axes de recherche majeur au LPS concernait alors le magnétisme des matériaux et leurs défauts, liés au désordre ou à la géométrie. Porté par une intuition « Toulousienne », Gérard s’était intéressé à une classification des défauts topologiques si bien qu’il produisit dans ce domaine des contributions majeures, appliquant ces concepts au domaine de la frustration et des verres de spins. Ma thèse d’état portant précisément sur les verres de spin, nous avons été amenés à interagir sur leur description thermodynamique. Gérard a quitté Orsay pour s’installer à l’ENS et je l’ai rejoint pour un semestre, en 1981, avant mon départ en post-doc à Berkeley. Je partageais alors un bureau avec Rammal.

J’ai toujours admiré chez Gérard sa capacité à sentir en amont les problèmes appelés à devenir « chauds », à les aborder par des approches transverses et à les résoudre de façon si élégante. Gérard avait en plus une qualité pédagogique remarquable. Il savait extraire l’essentiel des idées, en tirer le meilleur parti et les expliquer de façon claire. J’ajoute avoir eu le plaisir de partager quelques moments de convivialité avec lui, à son domicile, et également à la réception organisée à l’occasion de mon mariage!

## Acknowledgements

We benefited from numerous fruitful and valuable exchanges with colleagues at the DQMP department of the Université de Genève, especially Jean-Marc Triscone and Andrea Caviglia, at Thales, especially Manuel Bibes and also with Philippe Ghosez at the Université de Liège, Andrés Santander-Syro, Marcelo Rozenberg, Frédéric Piechon and Mark Goerbig at the Université Paris-Saclay. My grasp of materials science owes a lot to the late Professor Jacques Friedel whose remarkable and insightful course I took during my graduate years.

## Declaration of interests

The authors do not work for, advise, own shares in, or receive funds from any organization that could benefit from this article, and have declared no affiliations other than their research organizations.

## References

- [1] A. Ohtomo and H. Y. Hwang, “A high-mobility electron gas at the  $\text{LaAlO}_3/\text{SrTiO}_3$  heterointerface”, *Nature* **427** (2004), no. 6973, pp. 423–426.
- [2] N. Reyren, S. Thiel, A. D. Caviglia, et al., “Superconducting Interfaces Between Insulating Oxides”, *Science* **317** (2007), no. 5842, pp. 1196–1199.
- [3] J. A. Bert, B. Kalisky, C. Bell, M. Kim, Y. Hikita, H. Y. Hwang and K. A. Moler, “Direct imaging of the coexistence of ferromagnetism and superconductivity at the  $\text{LaAlO}_3/\text{SrTiO}_3$  interface”, *Nat. Phys.* **7** (2011), no. 10, pp. 767–771.
- [4] L. Li, C. Richter, J. Mannhart and R. C. Ashoori, “Coexistence of magnetic order and two-dimensional superconductivity at  $\text{LaAlO}_3/\text{SrTiO}_3$  interfaces”, *Nat. Phys.* **7** (2011), no. 10, pp. 762–766.
- [5] S. Banerjee, O. Erten and M. Randeria, “Ferromagnetic exchange, spin–orbit coupling and spiral magnetism at the  $\text{LaAlO}_3/\text{SrTiO}_3$  interface”, *Nat. Phys.* **9** (2013), pp. 626–630.
- [6] A. F. Santander-Syro, F. Fortuna, C. Bareille, et al., “Giant spin splitting of the two-dimensional electron gas at the surface of  $\text{SrTiO}_3$ ”, *Nature Mater.* **13** (2014), no. 12, pp. 1085–1090.
- [7] S. McKeown Walker, S. Riccò, F. Y. Bruno, et al., “Absence of Giant Spin Splitting in the Two-Dimensional Electron Liquid at the Surface of  $\text{SrTiO}_3$  (001)”, *Phys. Rev. B* **93** (2016), no. 24, article no. 245143.
- [8] T. Taniuchi, Y. Motoyui, K. Morozumi, T. C. Rödel, F. Fortuna, A. F. Santander-Syro and S. Shin, “Imaging of room-temperature ferromagnetic nano-domains at the surface of a non-magnetic oxide”, *Nat. Commun.* **7** (2016), pp. 11781–11786.
- [9] A. D. Caviglia, M. Gabay, S. Gariglio, N. Reyren, C. Cancellieri and J.-M. Triscone, “Tunable Rashba Spin-Orbit Interaction at Oxide Interfaces”, *Phys. Rev. Lett.* **104** (2010), no. 12, article no. 126803.
- [10] M. Ben Shalom, M. Sachs, D. Rakhmilevitch, A. Palevski and Y. Dagan, “Tuning Spin-Orbit Coupling and Superconductivity at the  $\text{SrTiO}_3/\text{LaAlO}_3$  Interface: A Magnetotransport Study”, *Phys. Rev. Lett.* **104** (2010), no. 12, article no. 126802.
- [11] A. D. Caviglia, S. Gariglio, N. Reyren, et al., “Electric field control of the  $\text{LaAlO}_3/\text{SrTiO}_3$  interface ground state”, *Nature* **456** (2008), no. 7222, pp. 624–627.
- [12] J. Varignon, L. Vila, A. Barthélémy and M. Bibes, “A new spin for oxide interfaces”, *Nat. Phys.* **14** (2018), no. 4, pp. 322–325.
- [13] Y.-Y. Pai, A. Tylan-Tyler, P. Irvin and J. Levy, “Physics of  $\text{SrTiO}_3$ -based heterostructures and nanostructures: a review”, *Rep. Prog. Phys.* **81** (2018), no. 3, article no. 036503.
- [14] A. Fert and F. Nguyen Van Dau, “Spintronics, from giant magnetoresistance to magnetic skyrmions and topological insulators”, *C. R. Phys.* **20** (2019), no. 7, pp. 817–831.
- [15] B. Förg, C. Richter and J. Mannhart, “Field-effect devices utilizing  $\text{LaAlO}_3$ - $\text{SrTiO}_3$  interfaces”, *Appl. Phys. Lett.* **100** (2012), no. 5, article no. 053506.
- [16] R. Jany, C. Richter, C. Woltmann, et al., “Monolithically Integrated Circuits from Functional Oxides”, *Adv. Mater. Interfaces* **1** (2014), no. 1, article no. 1300031.
- [17] D. G. Schlom and J. Mannhart, “Interface takes charge over Si”, *Nature Mater.* **10** (2011), no. 3, pp. 168–169.
- [18] H. Boschker and J. Mannhart, “Quantum-Matter Heterostructures”, *Ann. Rev. Cond. Matter Phys.* **8** (2017), no. 1, pp. 145–164.
- [19] T. C. Rödel, M. Vivek, F. Fortuna, et al., “Two-dimensional electron systems in  $\text{ATiO}_3$  perovskites ( $A = \text{Ca}, \text{Ba}, \text{Sr}$ ): Control of orbital hybridization and energy order”, *Phys. Rev. B* **96** (2017), article no. 041121.

- [20] P. Zubko, S. Gariglio, M. Gabay, P. Ghosez and J.-M. Triscone, "Interface Physics in Complex Oxide Heterostructures", *Ann. Rev. Cond. Matter Phys.* **2** (2011), no. 1, pp. 141–165.
- [21] D. Stornaiuolo, C. Cantoni, G. M. De Luca, et al., "Tunable spin polarization and superconductivity in engineered oxide interfaces", *Nature Mater.* **15** (2016), no. 3, pp. 278–8283.
- [22] J. Bréhin, Y. Chen, M. D'Antuono, et al., "Coexistence and coupling of ferroelectricity and magnetism in an oxide two-dimensional electron gas", *Nat. Phys.* **19** (2023), no. 6, pp. 823–829.
- [23] J. Mannhart and D. G. Schlom, "Oxide Interfaces — An Opportunity for Electronics", *Science* **327** (2010), no. 5973, pp. 1607–1611.
- [24] M. Salluzzo, "Electronic Reconstruction at the Interface Between Band Insulating Oxides: The LaAlO<sub>3</sub>/SrTiO<sub>3</sub> System", in *Oxide Thin Films, Multilayers, and Nanocomposites* (P. Mele, T. Endo, S. Arisawa, C. Li and T. Tsuchiya, eds.), Springer, 2015, pp. 181–211.
- [25] S. Gariglio, M. Gabay and J.-M. Triscone, "Research Update: Conductivity and beyond at the LaAlO<sub>3</sub>/SrTiO<sub>3</sub> interface", *APL Mater.* **4** (2016), article no. 060701.
- [26] V. N. Strocov, C. Cancellieri and A. S. Mishchenko, "Electrons and polarons at oxide interfaces explored by soft-X-ray ARPES", in *Spectroscopy of Complex Oxide Interfaces: Photoemission and Related Spectroscopies* (C. Cancellieri and V. N. Strocov, eds.), Springer, 2018, pp. 107–151.
- [27] G. Herranz, "Orbital Symmetry and Electronic Properties of Two-Dimensional Electron Systems in Oxide Heterointerfaces", in *Oxide Spintronics* (T. Banerjee, ed.), Jenny Stanford Publishing, 2019.
- [28] V. N. Strocov, A. Chikina, M. Caputo, et al., "Electronic phase separation at LaAlO<sub>3</sub>/SrTiO<sub>3</sub> interfaces tunable by oxygen deficiency", *Phys. Rev. Mater.* **3** (2019), no. 10, article no. 106001.
- [29] R. Pentcheva and W. E. Pickett, "Electronic phenomena at complex oxide interfaces: insights from first principles", *J. Phys. Cond. Matt.* **22** (2010), no. 4, article no. 043001.
- [30] P. García-Fernández, J. C. Wojdel, J. Íñiguez and J. A. Junquera, "Second-principles method for materials simulations including electron and lattice degrees of freedom", *Phys. Rev. B* **93** (2016), no. 19, article no. 195137.
- [31] O. Janson, Z. Zhong, G. Sangiovanni and K. Held, "Dynamical Mean Field Theory for Oxide Heterostructures", in *Spectroscopy of Complex Oxide Interfaces: Photoemission and Related Spectroscopies* (C. Cancellieri and V. N. Strocov, eds.), Springer, 2018, pp. 215–243.
- [32] A. E. M. Smink, J. C. de Boer, M. P. Stehno, A. Brinkman, W. G. van der Wiel and H. Hilgenkamp, "Gate-Tunable Band Structure of the LaAlO<sub>3</sub>–SrTiO<sub>3</sub> Interface", *Phys. Rev. Lett.* **118** (2017), no. 10, article no. 106401.
- [33] F. Stern, "Self-Consistent Results for *n*-Type Si Inversion Layers", *Phys. Rev. B* **5** (1972), no. 12, pp. 4891–4899.
- [34] T. C. Rödel, F. Fortuna, S. Sengupta, et al., "Universal Fabrication of 2D Electron Systems in Functional Oxides", *Adv. Mater.* **28** (2016), no. 10, pp. 1976–1980.
- [35] E. Frantzeskakis, T. C. Rödel, F. Fortuna and A. F. Santander-Syro, "2D surprises at the surface of 3D materials: Confined electron systems in transition metal oxides", *J. Electron Spectrosc. Relat. Phenom.* **219** (2017), pp. 16–28.
- [36] N. C. Plumb and M. Radović, "Angle-resolved photoemission spectroscopy studies of metallic surface and interface states of oxide insulators", *J. Phys. Cond. Matt.* **29** (2017), article no. 433005.
- [37] S. McKeown Walker, F. Y. Bruno and F. Baumberger, "ARPES Studies of Two-Dimensional Electron Gases at Transition Metal Oxide Surfaces", in *Spectroscopy of Complex Oxide Interfaces: Photoemission and Related Spectroscopies* (C. Cancellieri and V. N. Strocov, eds.), Springer, 2018, pp. 55–85.
- [38] S. Gariglio, A. D. Caviglia, J.-M. Triscone and M. Gabay, "A spin-orbit playground: surfaces and interfaces of transition metal oxides", *Rep. Prog. Phys.* **82** (2018), no. 1, article no. 012501.
- [39] Z. Zhong, Q. Zhang and K. Held, "Quantum confinement in perovskite oxide heterostructures: Tight binding instead of a nearly free electron picture", *Phys. Rev. B* **88** (2013), no. 12, article no. 125401.
- [40] G. Khalsa, B. Lee and A. H. MacDonald, "Theory of  $t_{2g}$  electron-gas Rashba interactions", *Phys. Rev. B* **88** (2013), article no. 041302.
- [41] M. Vivek, M. O. Goerbig and M. Gabay, "Topological states at the (001) surface of SrTiO<sub>3</sub>", *Phys. Rev. B* **95** (2017), article no. 165117.
- [42] P. Bruneel and M. Gabay, "Spin texture driven spintronic enhancement at the LaAlO<sub>3</sub>/SrTiO<sub>3</sub> interface", *Phys. Rev. B* **102** (2020), article no. 144407.
- [43] Y. A. Bychkov and E. I. Rashba, "Oscillatory effects and the magnetic susceptibility of carriers in inversion layers", *J. Phys. C: Solid State Phys.* **17** (1984), no. 33, pp. 6039–6045.
- [44] V. M. Edelstein, "Spin polarization of conduction electrons induced by electric current in two-dimensional asymmetric electron systems", *Solid State Comm.* **73** (1990), no. 3, pp. 233–235.
- [45] F. Gallego, F. Trier, S. Mallik, et al., "All-Electrical Detection of the Spin-Charge Conversion in Nanodevices Based on SrTiO<sub>3</sub>2–D Electron Gases", *Adv. Funct. Mater.* **34** (2024), no. 3, article no. 2307474.
- [46] X.-L. Qi and S.-C. Zhang, "Topological insulators and superconductors", *Rev. Mod. Phys.* **83** (2011), no. 4, pp. 1057–1110.
- [47] B. A. Bernevig and T. L. Hughes, *Topological Insulators and Topological Superconductors*, Princeton University Press, 2013.



- [48] K. Park, “A Passage to Topological Matter: Colloquium”, *J. Korean Phys. Soc.* **73** (2018), no. 6, pp. 817–832.
- [49] A. Haim and Y. Oreg, “Time-reversal-invariant topological superconductivity in one and two dimensions”, *Phys. Rep.* **825** (2019), pp. 1–48.
- [50] Y. Ando, “Topological Insulators”, 2023. *preprint*, arXiv:2307.14196.
- [51] B. Yan and C. Felser, “Topological Materials: Weyl Semimetals”, *Ann. Rev. Cond. Matter Phys.* **8** (2017), no. 1, pp. 337–354.
- [52] N. P. Armitage, E. J. Mele and A. Vishwanath, “Weyl and Dirac semimetals in three-dimensional solids”, *Rev. Mod. Phys.* **90** (2018), no. 1, article no. 015001.
- [53] B. A. Bernevig, T. L. Hughes and S.-C. Zhang, “Orbitronics: The Intrinsic Orbital Current in *p*-Doped Silicon”, *Phys. Rev. Lett.* **95** (2005), no. 6, article no. 066601.
- [54] B. A. Bernevig, T. L. Hughes and S.-C. Zhang, “Quantum Spin Hall Effect and Topological Phase Transition in HgTe Quantum Wells”, *Science* **314** (2006), no. 5806, pp. 1757–1761.
- [55] M. König, S. Wiedmann, C. Brüne, et al., “Quantum Spin Hall Insulator State in HgTe Quantum Wells”, *Science* **318** (2007), no. 5851, pp. 766–770.
- [56] Y. Tokura, M. Kawasaki and N. Nagaosa, “Emergent functions of quantum materials”, *Nat. Phys.* **13** (2017), pp. 1056–1068.
- [57] L. Chen, H. Hu, M. G. Vergniory, J. Cano and Q. Si, “Dirac zeros in an orbital selective Mott phase: Green’s function Berry curvature and flux quantization”, 2024. *preprint*, arXiv:2401.12156.
- [58] G. Khalsa and A. H. MacDonald, “Theory of the SrTiO<sub>3</sub> surface state two-dimensional electron gas”, *Phys. Rev. B* **86** (2012), no. 12, article no. 125121.
- [59] A. F. Santander-Syro, O. Copie, T. Kondo, et al., “Two-dimensional electron gas with universal subbands at the surface of SrTiO<sub>3</sub>”, *Nature* **469** (2011), pp. 189–93.
- [60] W. Meevasana, P. D. C. King, R. H. He, et al., “Creation and control of a two-dimensional electron liquid at the bare SrTiO<sub>3</sub> surface”, *Nature Mater.* **10** (2011), no. 2, pp. 114–118.
- [61] Z. Zhong, A. Tóth and K. Held, “Theory of spin-orbit coupling at LaAlO<sub>3</sub>/SrTiO<sub>3</sub> interfaces and SrTiO<sub>3</sub> surfaces”, *Phys. Rev. B* **87** (2013), no. 16, article no. 161102.
- [62] D. C. Vaz, P. Noël, A. Johansson, et al., “Mapping spin–charge conversion to the band structure in a topological oxide two-dimensional electron gas”, *Nature Mater.* **18** (2019), pp. 1187–1193.
- [63] P. D. C. King, S. McKeown Walker, A. Tamai, et al., “Quasiparticle dynamics and spin-orbital texture of the SrTiO<sub>3</sub> two-dimensional electron gas”, *Nat. Commun.* **5** (2014), no. 1, article no. 3414.
- [64] M. Altmeyer, H. O. Jeschke, O. Hijano Cubelos, et al., “Magnetism, Spin Texture, and In-Gap States: Atomic Specialization at the Surface of Oxygen-Deficient SrTiO<sub>3</sub>”, *Phys. Rev. Lett.* **116** (2016), no. 15, article no. 157203.
- [65] E. Lesne, Y. Fu, S. Oyarzun, et al., “Highly efficient and tunable spin-to-charge conversion through Rashba coupling at oxide interfaces”, *Nature Mater.* **15** (2016), pp. 1261–1266.
- [66] F. Trier, P. Noël, J.-V. Kim, J.-P. Attané, L. Vila and M. Bibes, “Oxide spin-orbitronics: spin–charge interconversion and topological spin textures”, *Nat. Rev. Mater.* **7** (2022), no. 4, pp. 258–274.
- [67] J. Sinova, S. O. Valenzuela, J. Wunderlich, C. H. Back and T. Jungwirth, “Spin Hall effects”, *Rev. Mod. Phys.* **87** (2015), no. 4, pp. 1213–1260.
- [68] F. Trier, D. C. Vaz, P. Bruneel, et al., “Electric-Field Control of Spin Current Generation and Detection in Ferromagnet-Free SrTiO<sub>3</sub>-Based Nanodevices”, *Nano Lett.* **20** (2020), no. 1, pp. 395–401.
- [69] A. Johansson, B. Göbel, J. Henk, M. Bibes and I. Mertig, “Spin and orbital Edelstein effects in a two-dimensional electron gas: Theory and application to SrTiO<sub>3</sub> interfaces”, *Phys. Rev. Res.* **3** (2021), no. 1, article no. 013275.
- [70] T. C. Rödel, C. Bareille, F. Fortuna, et al., “Orientational Tuning of the Fermi Sea of Confined Electrons at the SrTiO<sub>3</sub> (110) and (111) Surfaces”, *Phys. Rev. Applied* **1** (2014), no. 5, article no. 051002.
- [71] S. McKeown Walker, A. de la Torre, F. Y. Bruno, et al., “Control of a Two-Dimensional Electron Gas on SrTiO<sub>3</sub> (111) by Atomic Oxygen”, *Phys. Rev. Lett.* **113** (2014), article no. 177601.
- [72] K. Song, S. Ryu, H. Lee, et al., “Direct imaging of the electron liquid at oxide interfaces”, *Nat. Nanotechnol.* **13** (2018), no. 3, pp. 198–203.
- [73] D. Xiao, W. Zhu, Y. Ran, N. Nagaosa and S. Okamoto, “Interface engineering of quantum Hall effects in digital transition metal oxide heterostructures”, *Nat. Commun.* **2** (2011), article no. 596.
- [74] T. C. Rödel, C. Bareille, F. Fortuna, et al., “Orientational Tuning of the Fermi Sea of Confined Electrons at the SrTiO<sub>3</sub> (110) and (111) Surfaces”, *Phys. Rev. Appl.* **1** (2014), article no. 051002.
- [75] S. Okamoto and D. Xiao, “Transition-Metal Oxide (111) Bilayers”, *J. Phys. Soc. Jpn.* **87** (2018), no. 4, article no. 041006.
- [76] F. Simon, M. O. Goerbig and M. Gabay, “Normal state quantum geometry and superconducting domes in (111) oxide interfaces”, 2023. *preprint*, arXiv:2307.13993.
- [77] G. M. De Luca, R. Di Capua, E. Di Gennaro, et al., “Symmetry breaking at the (111) interfaces of SrTiO<sub>3</sub> hosting a two-dimensional electron system”, *Phys. Rev. B* **98** (2018), no. 11, article no. 115143.

- [78] A. Georges, L. de Medici and J. Mravlje, “Strong Correlations from Hund’s Coupling”, *Ann. Rev. Cond. Matter Phys.* **4** (2013), no. 1, pp. 137–178.
- [79] O. Hijano Cubelos, *Hétérostructures supraconductrices et isolants topologiques*, PhD thesis, Université Paris Saclay, Paris, France, 2015. <https://theses.hal.science/tel-01288200/>.
- [80] A. M. R. V. L. Monteiro, M. Vivek, D. J. Groenendijk, et al., “Band inversion driven by electronic correlations at the (111)  $\text{LaAlO}_3/\text{SrTiO}_3$  interface”, *Phys. Rev. B* **99** (2019), no. 20, article no. 201102.
- [81] U. Khanna, P. K. Rout, M. Mograbi, et al., “Symmetry and Correlation Effects on Band Structure Explain the Anomalous Transport Properties of (111)  $\text{LaAlO}_3/\text{SrTiO}_3$ ”, *Phys. Rev. Lett.* **123** (2019), no. 3, article no. 036805.
- [82] P. Bruneel, *Electronic and spintronic properties of the interfaces between transition metal oxides. Chapter 2*, PhD thesis, Université Paris-Saclay, Paris, France, 2020. <https://theses.hal.science/tel-03015119/>.
- [83] I. Sodemann and L. Fu, “Quantum Nonlinear Hall Effect Induced by Berry Curvature Dipole in Time-Reversal Invariant Materials”, *Phys. Rev. Lett.* **115** (2015), no. 21, article no. 216806.
- [84] E. Lesne, Y. G. Sağlam, R. Battilomo, et al., “Designing spin and orbital sources of Berry curvature at oxide interfaces”, *Nature Mater.* **22** (2023), no. 5, pp. 576–582.
- [85] M. T. Mercaldo, C. Noce, A. D. Caviglia, M. Cuoco and C. Ortix, “Orbital design of Berry curvature: pinch points and giant dipoles induced by crystal fields”, *npj Quantum Mater.* **8** (2023), no. 1, p. 12.
- [86] E. Lesne, Y. G. Sağlam, M. Kounalakis, M. Gabay, G. A. Steele and A. D. Caviglia, “Microwave spectroscopy of two-dimensional superconductivity at  $\text{LaAlO}_3/\text{SrTiO}_3$  (111) interfaces”, in *APS March Meeting 2021*, 2021.
- [87] A. Pezo, D. García Ovalle and A. Manchon, “Orbital Hall physics in two-dimensional Dirac materials”, *Phys. Rev. B* **108** (2023), no. 7, article no. 075427.
- [88] G. Tuvia, A. Burshtein, I. Silber, A. Aharony, O. Entin-Wohlman, M. Goldstein and Y. Dagan, “Enhanced Nonlinear Response by Manipulating the Dirac Point at the (111)  $\text{LaTiO}_3/\text{SrTiO}_3$  Interface”, *Phys. Rev. Lett.* **132** (2024), no. 14, article no. 146301.
- [89] P. He, S. McKeown Walker, S. S.-L. Zhang, et al., “Observation of Out-of-Plane Spin Texture in a  $\text{SrTiO}_3$  (111) Two-Dimensional Electron Gas”, *Phys. Rev. Lett.* **120** (2018), no. 26, article no. 266802.
- [90] F. Y. Bruno, S. McKeown Walker, S. Riccò, et al., “Band Structure and Spin-Orbital Texture of the (111)- $\text{KTaO}_3$  Two-Dimensional Electron Gas”, *Adv. Electron. Mater.* (2019), article no. 1800860.
- [91] F. Simon, M. Gabay, M. O. Goerbig and L. Pagot, “Role of the Berry curvature on BCS-type superconductivity in two-dimensional materials”, *Phys. Rev. B* **106** (2022), no. 21, article no. 214512.
- [92] S. Peotta and P. Törmä, “Superfluidity in topologically nontrivial flat bands”, *Nat. Commun.* **6** (2015), no. 1, article no. 8944.
- [93] E. Rossi, “Quantum metric and correlated states in two-dimensional systems”, *Curr. Opin. Solid State Mater. Sci.* **25** (2021), no. 5, article no. 100952.
- [94] P. Törmä, S. Peotta and B. A. Bernevig, “Superconductivity, superfluidity and quantum geometry in twisted multilayer systems”, *Nat. Rev. Phys.* **4** (2022), no. 8, pp. 528–542.
- [95] L. Liang, T. I. Vanhala, S. Peotta, T. Siro, A. Harju and P. Törmä, “Band geometry, Berry curvature, and superfluid weight”, *Phys. Rev. B* **95** (2017), no. 2, article no. 024515.
- [96] H. Tian, X. Gao, Y. Zhang, et al., “Evidence for Dirac flat band superconductivity enabled by quantum geometry”, *Nature* **614** (2023), no. 7948, pp. 440–444.
- [97] P. K. Rout, E. Maniv and Y. Dagan, “Link between the Superconducting Dome and Spin-Orbit Interaction in the (111)  $\text{LaAlO}_3/\text{SrTiO}_3$  Interface”, *Phys. Rev. Lett.* **119** (2017), no. 23, article no. 237002.